

**UNDERWATER ACOUSTIC NOISE  
GENERATION AND PROPAGATION  
RESULTING FROM PILE DRIVING FOR  
OREGON BRIDGE CONSTRUCTION**

**Final Report**

**SPR 731**



Oregon Department of Transportation



**UNDERWATER ACOUSTIC NOISE GENERATION AND  
PROPAGATION RESULTING FROM PILE DRIVING FOR  
OREGON BRIDGE CONSTRUCTION**

**Final Report**

**SPR 731**

by

Lisa M. Zurk, T. Martin Siderius, Nathan Laws, and Scott Schecklman  
Electrical and Computer Engineering Department  
Portland State University  
1900 SW Fourth, FAB 160-17  
Portland, OR 97207

for

Oregon Department of Transportation  
Research Section  
555 13<sup>th</sup> Street, Suite 1  
Salem OR 97301

and

Federal Highway Administration  
400 Seventh Street, SW  
Washington, DC 20590-0003

**June 2014**



1. Report No. FHWA-OR-RD-14-13		2. Government Accession No.		3. Recipient's Catalog No.	
4. Title and Subtitle Underwater Acoustic Noise Generation and Propagation Resulting from Pile Driving for Oregon Bridge Construction				5. Report Date -month- -year-	
				6. Performing Organization Code	
7. Author(s) Lisa M. Zurk, T. Martin Siderius, Nathan Laws, and Scott Schecklman Electrical and Computer Engineering Department, Portland State University				8. Performing Organization Report No.  SPR 731	
9. Performing Organization Name and Address Oregon Department of Transportation Research Section 555 13 <sup>th</sup> Street, Suite 1 Salem, OR 97301				10. Work Unit No. (TRAIS)	
				11. Contract or Grant No.  SPR 731	
12. Sponsoring Agency Name and Address Oregon Department of Transportation Research Section and Federal Highway Administration 555 13 <sup>th</sup> Street, Suite 1 400 Seventh Street, SW Salem, OR 97301-5192 Washington, DC 20590-0003				13. Type of Report and Period Covered Final Report	
				14. Sponsoring Agency Code	
15. Supplementary Notes					
16. Abstract There is growing concern about noise levels from pile driving activities associated with the construction of highway bridges and other in-water structures. It has been demonstrated that noise generated from pile driving with an impact hammer can be harmful to aquatic species protected by the state and federal Endangered Species Act (ESA). To comply with current environmental regulations and noise level attenuation criteria, ODOT needs to develop hydro-acoustic monitoring protocol and predictive models so projects can develop appropriate sound attenuation strategies based on site specific conditions. This research project addresses several concerns related to hydro-acoustic impacts and will ultimately help highway projects stay in compliance with established noise level criteria. The research project included: 1) identification of sound generation mechanisms from pile driving and how sound propagates into the surrounding underwater environment, 2) development of an acoustic monitoring procedure and predictive model that will help assure compliance and 3) validation and verification of predictive models.					
17. Key Words PILE DRIVING, ACOUSTIC, PROPAGATION MODEL			18. Distribution Statement Copies available from NTIS, and online at <a href="http://www.oregon.gov/ODOT/TD/TP_RES/">http://www.oregon.gov/ODOT/TD/TP_RES/</a>		
19. Security Classification (of this report) Unclassified		20. Security Classification (of this page) Unclassified		21. No. of Pages 78	22. Price

## SI\* (MODERN METRIC) CONVERSION FACTORS

APPROXIMATE CONVERSIONS TO SI UNITS					APPROXIMATE CONVERSIONS FROM SI UNITS				
Symbol	When You Know	Multiply By	To Find	Symbol	Symbol	When You Know	Multiply By	To Find	Symbol
<b><u>LENGTH</u></b>					<b><u>LENGTH</u></b>				
in	inches	25.4	millimeters	mm	mm	millimeters	0.039	inches	in
ft	feet	0.305	meters	m	m	meters	3.28	feet	ft
yd	yards	0.914	meters	m	m	meters	1.09	yards	yd
mi	miles	1.61	kilometers	km	km	kilometers	0.621	miles	mi
<b><u>AREA</u></b>					<b><u>AREA</u></b>				
in <sup>2</sup>	square inches	645.2	millimeters squared	mm <sup>2</sup>	mm <sup>2</sup>	millimeters squared	0.0016	square inches	in <sup>2</sup>
ft <sup>2</sup>	square feet	0.093	meters squared	m <sup>2</sup>	m <sup>2</sup>	meters squared	10.764	square feet	ft <sup>2</sup>
yd <sup>2</sup>	square yards	0.836	meters squared	m <sup>2</sup>	m <sup>2</sup>	meters squared	1.196	square yards	yd <sup>2</sup>
ac	acres	0.405	hectares	ha	ha	hectares	2.47	acres	ac
mi <sup>2</sup>	square miles	2.59	kilometers squared	km <sup>2</sup>	km <sup>2</sup>	kilometers squared	0.386	square miles	mi <sup>2</sup>
<b><u>VOLUME</u></b>					<b><u>VOLUME</u></b>				
fl oz	fluid ounces	29.57	milliliters	ml	ml	milliliters	0.034	fluid ounces	fl oz
gal	gallons	3.785	liters	L	L	liters	0.264	gallons	gal
ft <sup>3</sup>	cubic feet	0.028	meters cubed	m <sup>3</sup>	m <sup>3</sup>	meters cubed	35.315	cubic feet	ft <sup>3</sup>
yd <sup>3</sup>	cubic yards	0.765	meters cubed	m <sup>3</sup>	m <sup>3</sup>	meters cubed	1.308	cubic yards	yd <sup>3</sup>
NOTE: Volumes greater than 1000 L shall be shown in m <sup>3</sup> .									
<b><u>MASS</u></b>					<b><u>MASS</u></b>				
oz	ounces	28.35	grams	g	g	grams	0.035	ounces	oz
lb	pounds	0.454	kilograms	kg	kg	kilograms	2.205	pounds	lb
T	short tons (2000 lb)	0.907	megagrams	Mg	Mg	megagrams	1.102	short tons (2000 lb)	T
<b><u>TEMPERATURE (exact)</u></b>					<b><u>TEMPERATURE (exact)</u></b>				
°F	Fahrenheit	(F-32)/1.8	Celsius	°C	°C	Celsius	1.8C+32	Fahrenheit	°F

\*SI is the symbol for the International System of Measurement

## **ACKNOWLEDGEMENTS**

The research included in this report was sponsored by the Oregon Department of Transportation (ODOT). The project team would like to thank the research staff at ODOT and the members of the Technical Advisory Committee for their oversight and guidance in the performance of this research effort. Sharon Rainsberry from the Environmental Services Office of the Washington State Department of Transportation and Steve Morrow from the Columbia River Crossing (CRC) project provided valuable information about the environment surrounding the proposed pile driving activity to build a new I-5 bridge between Oregon and Washington. The project team would also like to thank the Marine Services Division of David Evans and Associates, Inc. in Vancouver, WA for recording pile driving noise data from test piles in the Columbia River. Ben Hocker, Nicholas Lesnikowski and James Coleman were especially helpful in providing local bathymetry data, and recording and post-processing the hydro-acoustic recordings.

## **DISCLAIMER**

This document is disseminated under the sponsorship of the Oregon Department of Transportation and the United States Department of Transportation in the interest of information exchange. The State of Oregon and the United States Government assume no liability of its contents or use thereof.

The contents of this report reflect the view of the authors who are solely responsible for the facts and accuracy of the material presented. The contents do not necessarily reflect the official views of the Oregon Department of Transportation or the United States Department of Transportation.

The State of Oregon and the United States Government do not endorse products of manufacturers. Trademarks or manufacturers' names appear herein only because they are considered essential to the object of this document.

This report does not constitute a standard, specification, or regulation.



# TABLE OF CONTENTS

<b>EXECUTIVE SUMMARY .....</b>	<b>1</b>
<b>1.0 INTRODUCTION.....</b>	<b>3</b>
1.1 OBJECTIVES .....	3
1.2 BENEFITS .....	3
1.3 BACKGROUND AND SIGNIFICANCE OF WORK.....	3
1.4 IMPLEMENTATION .....	4
1.5 RESEARCH TASKS .....	4
<b>2.0 PROJECT TASK REVIEW .....</b>	<b>5</b>
2.1 TASK 1: LITERATURE REVIEW .....	5
2.2 TASK 2: PILE DRIVING SOURCE MODELS .....	5
2.3 TASK 3: MODELING SOUND PROPAGATION.....	5
2.4 TASK 4: NATURAL ATTENUATION MECHANISMS.....	5
2.5 TASK 5: MONITORING FOR COMPLIANCE AND MODEL VALIDATION .....	6
2.6 TASK 6: SITE CHARACTERIZATION.....	6
2.7 TASK 7: ANALYSIS OF MODELING AND DATA .....	6
<b>3.0 MODELING SOUND PROPAGATION.....</b>	<b>7</b>
3.1 SHALLOW WATER SOUND PROPAGATION.....	7
3.2 PARABOLIC EQUATION (PE) PROPAGATION.....	10
3.3 FREQUENCY SYNTHESIS.....	12
3.4 GEOACOUSTIC MODEL.....	14
<b>4.0 MODELING THE PILE DRIVING SOURCE.....</b>	<b>19</b>
4.1 EMPIRICAL SOURCE MODEL .....	19
4.2 FDTD SOURCE MODEL.....	23
4.3 DISCUSSION .....	26
<b>5.0 MODEL VALIDATION .....</b>	<b>29</b>
5.1 EXPERIMENTAL DATA .....	29
5.2 SIMULATION CONFIGURATION .....	31
5.3 MEASUREMENT METRICS .....	33
5.4 POWER SPECTRAL DENSITY AND SOUND PRESSURE LEVEL COMPARISONS .....	34
5.5 SOUND EXPOSURE LEVEL COMPARISONS .....	43
<b>6.0 MODEL APPLICATIONS AND SITE CHARACTERIZATION .....</b>	<b>45</b>
6.1 CONTOUR PLOTS.....	45
6.2 CHARACTERIZATION OF BATHYMETRY VARIATIONS .....	47
6.3 CHARACTERIZATION OF SEDIMENT CONFIGURATIONS.....	49
<b>7.0 CONCLUSION .....</b>	<b>55</b>
<b>8.0 REFERENCES.....</b>	<b>57</b>

**APPENDIX A - MODEL IMPLEMENTATION**  
**APPENDIX B - RAM-PE CONVERGENCE**

**LIST OF TABLES**

Table 3.1: Summary of Geoacoustic Parameters ..... 16  
Table 5.1: Test Pile Model Parameters ..... 32  
Table 5.2: Sound Exposure Level Summary. All entries are in units of dB re:  $1\mu\text{Pa}^2\text{s}$ . ..... 43  
Table 6.1: Parameters for Top Sediment Layer Comparison ..... 51

# LIST OF FIGURES

Figure 3.1: Illustration of the reflected and transmitted waves produced by an acoustic wave incident across a boundary between two media. Each boundary has distinct sound speeds ( $c$ ) and densities ( $\rho$ ). A portion of the wave is reflected at the angle of incidence ( $\theta_i$ ), and a portion is transmitted at the transmission angle, ( $\theta_t$ ). .....8

Figure 3.2: Possible multipath interactions between an arbitrary source and receiver. Illustrated are 1) the direct path, 2) the air-water interface reflected path, 3) the water-sediment reflected path, 4) the path transmitted through sediment 1 and reflected from sediment 2, and 5) the water-air, water-sediment, and water-air reflected path. The dotted arrows highlight the reflected or transmitted portion of the waveform that does not reach the receiver.....9

Figure 3.3: Practical spreading model solutions for F parameters of 5, 10, and 15 with a source level of 210 dB. ....10

Figure 3.4: Example RAM-PE solution. SPL is plotted as a function of range and depth through multiple sediment layers ..... 11

Figure 3.5: Example coring sample taken of the Troutdale Formation under the Columbia River. .... 14

Figure 3.6: Columbia River Bathymetry between Portland, OR and Vancouver WA, obtained from NOAA fathometer measurements. The gray scale represents river depth and the areas of zero depth at figure center correspond to the existing I5 span..... 15

Figure 3.7: The sediment layers used in the model. The arrows on the right of the figure indicate the variability in each sediment layer. The Troutdale Formation represents the acoustic basement and is effectively of infinite depth..... 16

Figure 3.8: Sound speed profiles for sites A and B. The lower sound speed regions at shallow depth correspond to the sand layer, the rapid transition corresponds to the narrow gravel layer, and the high sound speed region corresponds to the Troutdale Formation. .... 17

Figure 4.1: The arrivals of the empirical source model. Panels (a), (b), and (c) show the bulge traveling through the pile and the emitted arrivals at progressively later times.  $c_p$  is the speed of sound in the pile and  $\phi_w$  is the arrival angle in the water,  $\phi_s$  is the arrival angle in the sediment, and  $\phi_{ws}$  is the angle of the arrival that originated in the sediment and transitioned to the water. .... 20

Figure 4.2: Empirically observed pile driving waveform resulting from a 10 meter observation of pile B1. Receiver is at 3.75 meter depth. .... 22

Figure 4.3: Example spectral weight function formulated from an empirical observation of a hammer impact on pile B1 ..... 22

Figure 4.4: First arrival isolated from the empirical waveform. Samples not corresponding to the first arrival have been discarded..... 23

Figure 4.5: Illustration of the FDTD Source Model, and the coupling into the propagation model. The cylindrical shells on the left represent the nodal particle velocity solutions of radius  $a$  and height  $dz$ . The  $N$  particle velocity nodes are converted to  $N$  simple sources and convolved with the RAM-PE Green's functions solutions, represented by red dots at right. .... 24

Figure 4.6: Short-range propagation still frames using the empirical source model to represent pile B1. The angled waves were emitted from the pile for a time period that included 4 arrivals. The black lines demarcate the sediment layer boundaries. The top layer is the water column, followed by sand, gravel and the Troutdale Formation, descending downward. .... 27

Figure 4.7: Short-range propagation still frames using the FDTD source model to represent pile B1. The lines demarcate the sediment layer boundaries. The top layer is the water column, followed by sand, gravel and the Troutdale Formation, descending downward. .... 28

Figure 5.1: Test pile locations in pile sites A and B located in the path of the proposed new I5 span. Piles B1 and A1 are 24 inch diameter piles and Piles B2 and A3 are 48 inch diameter piles. Grayscale corresponds to water depth..... 29

Figure 5.2: Test pile monitoring locations. Observations along the north riverside correspond to pile site B, and those along the south riverside correspond to pile site A. Grayscale corresponds to water depth. .... 30

Figure 5.3: Data record of pile driving impacts on test pile B1 taken at 10m from the pile location. Impacts are shown as SPL. .... 30

Figure 5.4: Example acoustic data from pile B1. Panel (A) shows the average time domain waveform from the 10 m monitoring location. Panel (B) shows the SEL computed from the waveform in Panel (A), and Panel (C) plots the PSD calculated from observations from 10 to 800 meters from the test pile site..... 31

Figure 5.5: Spectral weight functions for each pile. All weight functions are derived from observations taken at 10 m from the corresponding test piles. ....	32
Figure 5.6: PSD comparisons for pile B1. Panel A corresponds to the 10m Observation site, B to 200m, C to 400m, D to 800m, and E to the 800m site in the opposite direction. ....	35
Figure 5.7: PSD comparisons for pile B2. Panel A corresponds to the 10m Observation site, B to 200m, C to 400m, D to 800m, and E to the 800m site in the opposite direction. ....	36
Figure 5.8: PSD comparisons for pile A1. Panel A corresponds to the 10m Observation site, B to 200m, C to 400m, D to 800m, and E to the 800m site in the opposite direction. ....	37
Figure 5.9: PSD comparisons for pile A3. Panel A corresponds to the 10m Observation site, B to 200m, C to 400m, D to 800m, and E to the 800m site in the opposite direction. ....	38
Figure 5.10: SPL comparisons for pile B1. Panel A corresponds to the 10m Observation site, B to 200m, C to 400m, D to 800m, and E to the 800m site in the opposite direction. ....	39
Figure 5.11: SPL comparisons for pile B2. Panel A corresponds to the 10m Observation site, B to 200m, C to 400m, D to 800m, and E to the 800m site in the opposite direction. ....	40
Figure 5.12: SPL comparisons for pile A1. Panel A corresponds to the 10m Observation site, B to 200m, C to 400m, D to 800m, and E to the 800m site in the opposite direction. ....	41
Figure 5.13: SPL comparisons for pile A3. Panel A corresponds to the 10m Observation site, B to 200m, C to 400m, D to 800m, and E to the 800m site in the opposite direction. ....	42
Figure 5.14: Sound exposure level summaries for each pile. The dotted lines correspond to results using the practical spreading model. The top line corresponds to an F factor of 5 and the bottom an F of 20. The middle line is a fit to the data, and corresponds to an F of 10.5. ....	44
Figure 6.1: SEL contour plot about pile B1. The radial lines demarcate two-dimensional simulation results, and the lines connecting radials connect points of equivalent SEL. ....	46
Figure 6.2: SEL contour plot about pile A3. The radial lines demarcate two-dimensional simulation results, and the lines connecting radials connect points of equivalent SEL. ....	47
Figure 6.3: Five bathymetry test cases, located near the I-5 Columbia River crossing. Test cases encompass the deep and shallow extremes, as well as the extremes for roughness and sloping bottoms found in the neighborhood of the construction site. Test cases are taken from the Bathymetry at center and correspond to the labeled arrows. ....	48
Figure 6.4: Range dependent SEL at a depth of 3.5m, for each bathymetry test case. ....	48
Figure 6.5: Statistical threshold plot comparing the percent of the water column SEL above certain thresholds, for the different test cases. The region of comparison comprises the water column from range 100m to 200m. ....	49
Figure 6.6: Range dependent SEL at 3.5 meter depth for multiple bedrock depths about pile B1. X demarcates the acoustic observations. Bedrock depths are relative to the simulation bathymetry. ....	50
Figure 6.7: Statistical threshold plot comparing the percentage of the water column above certain SELs, for several bedrock depths. Again, variations in a shallow bedrock layer have the greatest effect, and bedrocks below 25 meter depth have little practical effect on the water column SEL. The region of consideration is the water column from range 100 to 200 meters. ....	50
Figure 6.8: Range dependent SEL at 3.5m depth, for the top layer compositions in Table 6.1, about pile A3. X marks the observed SEL. ....	52
Figure 6.9: Statistical threshold plot comparing the percentage of the water column about certain SEL, for each top layer composition. The area of interest is the water column from range 100 to 200 meters. ....	52
Figure 6.10: Geometrical explanation for the large SEL spike seen around 370 m in Figure 6.8. The propagation angle is assumed to change very little in the sediment due to the similar sound speeds. ....	53

## EXECUTIVE SUMMARY

There is growing concern about noise levels from pile driving activities associated with the construction of highway bridges and other in-water structures. It has been demonstrated that noise generated from pile driving with an impact hammer can be harmful to aquatic species protected by the state and federal Endangered Species Act (ESA). To comply with current environmental regulations and noise level attenuation criteria, ODOT needs to develop hydro-acoustic monitoring protocol and predictive models so projects can develop appropriate sound attenuation strategies based on site specific conditions.

This research project addresses several concerns related to hydro-acoustic impacts and will ultimately help highway projects stay in compliance with established noise level criteria. The research project included: 1) identification of sound generation mechanisms from pile driving and how sound propagates into the surrounding underwater environment, 2) development of an acoustic monitoring procedure and predictive model that will help assure compliance and 3) validation and verification of predictive models.

The research project was initially divided into ten tasks to be completed in three phases over a two year time frame. In addition to quarterly reports, incremental reports were also submitted to ODOT at the end of Phase 1 in June 2011 and Phase 2 in July 2011. A progress report was presented to the TAC members at the ODOT Research Section Library on June 6, 2012. This final report summarizes the key objectives and results for the entire research effort.

In addition to sponsor status reports, this research project contributed to the advancement of scientific knowledge in the underwater acoustics community. Pile driving measurement and modeling results were discussed by Prof. Martin Siderius during a poster presentation entitled “Challenges in the Quantitative Assessment of Anthropogenic Sound in Marine Environments” at the Fisheries Workshop poster session during the 161st Meeting of the Acoustical Society of America in Seattle WA in May 2011. On October 27, 2012 Nathan Laws presented “Numerically Predicting Impact Pile Driving Noise in Shallow, Inhomogeneous Channels” at the Special Session on Pile Driving during the 164th Meeting of the Acoustical Society of America in Kansas City, MO. A peer-reviewed journal publication is currently in preparation for publication in the Journal of the Acoustical Society of America (JASA) in the summer of 2013.

Finally, this research enhanced the educational experience for college students studying underwater acoustics within the State of Oregon. Several graduate students at Portland State University participated in field experiments by deploying and retrieving hydrophone sensors in the Columbia River. The sensors (some of which were built by the students) were used to record ambient and background noise levels. The students then post-processed the recorded data with computer code which they had written. This research project also served as a Master’s degree thesis topic in the Electrical and Computer Engineering Department. During the past two years Prof. Lisa Zurk served as advisor to Nathan Laws who successfully defended his thesis entitled,

“A Parabolic Equation Synthesis to Account for the Noise Radiated by Underwater Impact Pile Driving” on February 6, 2013.

## **1.0 INTRODUCTION**

There is growing concern about noise levels from pile driving activities associated with the construction of highway bridges and other in-water structures. It has been demonstrated that noise generated from pile driving with an impact hammer can be harmful to aquatic species protected by the state and federal Endangered Species Act (ESA) (*Hardyniec and Skeen 2005, Hastings and Popper 2005*). Construction activities in Oregon are subject to compliance with established noise level criteria (cited as a single strike peak of 206 dB, and for cumulative strikes, 187 dB sound exposure level (SEL) in areas and at times where fish are larger than 2 grams and 183 dB SEL in areas and at times when fish are smaller than 2 grams). ODOT's first efforts at mitigating underwater pile driving noise have been costly and problematic.

### **1.1 OBJECTIVES**

This research project addresses several concerns related to hydro-acoustic impacts and ultimately assists highway projects in compliance with established noise level criteria. The research project included: 1) identifying sound generation mechanisms from pile driving and how sound propagates and naturally attenuates in the surrounding underwater environment, 2) develop an acoustic monitoring procedure and predictive model that would help assure compliance and 3) conduct validation and verification of predictive models.

In summary, the goal of the research project was to develop predictive modeling capability. This modeling capability may be used to estimate expected sound levels due to various pile driving activities at specific locations. With that information, site specific recommendations can be made regarding attenuation strategies, taking into account the sound generation and propagation effects. This would allow highway projects to implement the appropriate level of hydro-acoustic attenuation, based on site specific conditions, assure regulatory compliance, and achieve better cost efficiencies. Bridge construction activities and associated monitoring that is occurring in Oregon provides a unique opportunity to engage the scientific community with the goal of improving our understanding and management of human generated underwater acoustic noise.

### **1.2 BENEFITS**

A model to predict sound levels for specific projects allows engineers to design attenuation appropriate for the project. Ultimately, knowledge of the necessary attenuation during project development will save time and money and demonstrate good environmental stewardship.

### **1.3 BACKGROUND AND SIGNIFICANCE OF WORK**

Regulatory demands related to pile driving noise have emerged recently and quickly. While there exists older work related to the effect of explosions on fish, these regulations emerged onto a scene where essentially no prior work had been done on hydro-acoustic noise from pile driving. Most hydro-acoustic research completed to date has been done in deep water habitat with large (8 foot) diameter piles, e.g. San Francisco Bay and Puget Sound. Additionally, there is a related

situation where there appears to be a paucity of expertise available to provide the services needed for compliance.

Typically, ODOT projects are completed in shallow riverine or estuarine environments with smaller (4 foot) diameter piles. This means that the small, recent body of research that was available is not directly applicable. It also means that some of the mitigation measures that had previously been developed were not as amenable to ODOTs projects.

To comply with current environmental regulations and noise level attenuation criteria, ODOT needs to develop hydro-acoustic monitoring protocols and predictive models so projects can develop appropriate sound attenuation strategies based on site specific conditions.

## **1.4 IMPLEMENTATION**

The algorithms which have been developed include a monitoring protocol and predictive model for assessing expected hydro-acoustic sound pressure levels resulting from pile driving. This information may be used by project teams to develop appropriate hydro-acoustic monitoring and mitigation strategies to help ODOT projects stay in compliance with current design criteria and environmental regulations without disrupting construction schedules.

## **1.5 RESEARCH TASKS**

The project was initially broken up into a total of ten research tasks, which are discussed in detail in Chapter 2. During Task 8 researchers from Portland State University deployed hydro-acoustic sensors in the Columbia River (in January and March of 2011) to measure background and ambient noise in vicinity of pile driving completed as part of the I-5 Columbia River Crossing (CRC) project. The data collection methodology and measurement results were documented in a final report to the CRC commission and ODOT in April 2011. Task 9 would have been to monitor sound levels from pile driving tests near the proposed I-5 Columbia River Crossing were conducted February 11-21, 2011. Before the research project started, this task was removed from the PSU research project list and assigned to David Evans and Associates (DEA). The hydro-acoustic noise data recorded by DEA were used by researchers at PSU to support the research efforts in Tasks 2 - 7.

This final report constitutes Task 10 which was to compile the results of each of the research tasks. Since the results of Task 8 were fully documented in a previous report, those results will not be repeated here. The following chapter provides a more in-depth overview of results from research tasks 1 - 7. Subsequent chapters show more detailed modeling equations, data analysis and results.

## **2.0 PROJECT TASK REVIEW**

### **2.1 TASK 1: LITERATURE REVIEW**

Dr. Mardi Hastings at the Georgia Institute of Technology (GTech) provided a literature of survey of the current research surrounding pile driving under sub-contract with the NEAR-Lab for this project. The review encompassed 53 sources covering recent developments in the effects of pile driving on marine animals as well as methods of characterizing and mitigating pile driving sound. The review was submitted on December 17, 2011 under subcontract 201ZUR269.

### **2.2 TASK 2: PILE DRIVING SOURCE MODELS**

Two contrasting models of the pile driving source were adapted from recent developments in the technical literature, which result in models of the pile source that can be implemented based on different input parameters. These source models were an empirical model adapted from the work of Reinhall and Dahl (2011) and an FDTD model from Shahab and Hastings (2011) at GTech. The FDTD model was developed under sub-contract with the NEAR-Lab, and the researchers at GTech were only able to provide preliminary results for a single pile. Both source models were adapted to be used in a model of shallow water propagation, which included the derivation of a virtual source array for the FDTD source model.

### **2.3 TASK 3: MODELING SOUND PROPAGATION**

Parabolic Equation (PE) wave propagation techniques (*Jensen et al. 1994*) were used to model physics based wave propagation in the shallow water environments where pile driving typically occurs. PE propagation was carried out using convergent results from a modified version of the range-dependent acoustic model (RAM-PE), a publicly available PE code (*Collins 1993*). The model of propagation allows range dependent bathymetry variations and arbitrarily complex sediment configurations. The propagation model was implemented using bathymetry and a sediment model corresponding to the Columbia River in the vicinity of the proposed I5 span.

### **2.4 TASK 4: NATURAL ATTENUATION MECHANISMS**

The attenuation of the pile driving source was accounted for as a combination transmission loss (TL) from both spreading and sediment losses. Spreading loss depends on the distance from the pile and bathymetry, and sediment loss is dependent upon the bathymetry and sediment composition. Sediment were accounted for by the use of bathymetry from the Columbia River and the derivation of a linear sediment geoacoustic model, which produced superior sound level predictions as compared to nonlinear models for the sandy sediment composition of the Columbia River. The effects of bathymetry, top sediment layer composition, and bedrock position were analyzed as an extension of the computational model. In general, deeper water was shown to result in less attenuation, although variations in bathymetry from shallow to deeper

areas can result in local rapid attenuation. Higher density and sound speed sediment layers result in less bottom losses.

## **2.5 TASK 5: MONITORING FOR COMPLIANCE AND MODEL VALIDATION**

Simulated results were compared to acoustic observations of test pile operations taken in the Columbia River in February of 2011 by David Evans and Associates. Simulations were performed to match the acoustic observations which encompassed various pile types and sediment configurations. Comparisons showed good agreement in sound pressure level (SPL), power spectral density (PSD), and sound exposure level (SEL) comparisons that were made to a distance of 800 m from the pile driving source. Agreement is excellent within 400m of the pile source.

## **2.6 TASK 6: SITE CHARACTERIZATION**

Detailed bathymetry data was obtained from David Evans and Associates and sediment type, layer, and thickness were taken from geotechnical survey data in the Columbia River, obtained from the CRC. This data was used to derive a linear geoacoustic model of the Columbia River sediment based on the viscoelastic model of Hamilton (1980)(DEA 2011). Variations in the bathymetry and sediment configurations were analyzed by comparing modeling results that spanned the extremes of both the sediment and bathymetry variations in the Columbia River. Furthermore the model was extended to create contour sound level predictions over large areas of the Columbia River.

Dr. Mardi Hastings at GTech was also subcontracted to provide species sensitivities to the effects of pile driving in Oregon's marine habitats. This report has not been provided at the time of this writing.

## **2.7 TASK 7: ANALYSIS OF MODELING AND DATA**

Significant code was developed to both carry out the computational model and analyze results. A main propagation routine was developed to calculate propagation using a specified source model, geoacoustic configuration, and bathymetry for the Columbia River. Pre- and post-processing routines were developed to implement the empirical and FDTD source models respectively with the propagation routine.

Capabilities were developed to analyze this data which included code to process acoustic observations and make comparisons in SPL, SEL, and PSD at several locations. Furthermore code was developed to predict sound levels over large areas of the Columbia River and analyze variations in bathymetry and sediment configuration in both sound level contours and statistical thresholds. Finally, code was developed to analyze time domain propagation as a movie.

### 3.0 MODELING SOUND PROPAGATION

The intent of this chapter is to present the qualitative and mathematical content necessary to understand how acoustic propagation is accounted for in this modeling work. Pile driving typically occurs in shallow water environments, where bathymetry and sediment variations significantly affect transmission loss (TL) and propagation characteristics. Computation of physics-based wave propagation through shallow water environments is accomplished through the application of parabolic equation (PE) propagation techniques, and is carried out using the publicly available code, the RAM-PE. Since the RAM-PE computes propagation at only a single frequency per execution, the formulations used in the broadband synthesis of a time domain solution are presented. Finally, the derivation of the geoaoustic model is shown along with the specific parameters used to model the specific sediment of the Columbia River.

#### 3.1 SHALLOW WATER SOUND PROPAGATION

The propagation of acoustic waves in shallow water differs from other forms of acoustic propagation, such as in air or deep water, by the presence of boundaries that significantly affect sound propagation characteristics. These boundaries form an acoustic waveguide (*Jensen et al. 1994*), which produces complex modal interference patterns in the water column. A detailed discussion of underwater propagation is beyond the scope of this report, so the reader is referred to the standard text, *Computational Ocean Acoustics (Jensen et al. 1994)*. This report will provide a discussion of the reflection and multipath dynamics that lead to the interference patterns, which should give a better intuitive understanding of the model. Finally, the sources of transmission loss (TL) and how they relate to the shallow water environment are discussed.

Boundaries to acoustic propagation are formed by the air-water interface as well as the sediment layers, all of which cause reflections and multipath interactions. The air water interface is considered a perfectly reflecting surface, with all acoustic energy incident reflected back into the water. This is not the case for sediment reflections, where the incident wave is divided into reflected and transmitted parts (*Jensen et al. 1994*), shown in Figure 3.1. The portions of the of the wave transmitted and reflected are proportional to the reflection coefficient,

$$R = \frac{Z_2 - Z_1}{Z_2 + Z_1} \quad (3.1)$$

and the transmission coefficient,

$$T = \frac{2Z_2}{Z_2 + Z_1} \quad (3.2)$$

Both coefficients are ratios of the impedances between the media. The impedance of the  $i^{\text{th}}$  medium is,

$$Z_i = \frac{\rho_i c_i}{\sin \theta_i} \quad (3.3)$$

where  $c_i$  and  $\rho_i$  are the sound speed and density in the  $i^{\text{th}}$  medium. The angle of reflection is equivalent to the incidence angle,  $\theta_1$ , and the angle of transmission is governed by Snell's Law,

$$\frac{\omega}{c_1} \sin \theta_1 = \frac{\omega}{c_2} \sin \theta_2 \quad (3.4)$$

where  $\omega$  is the angular frequency of the incident wave.

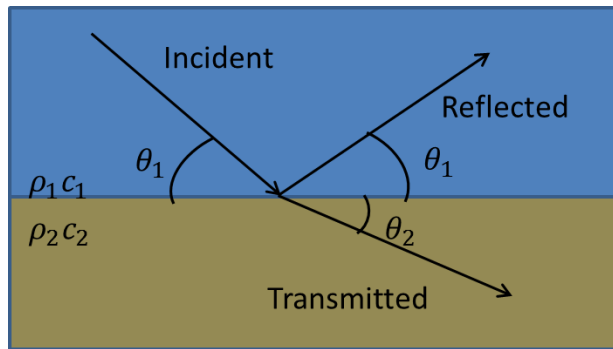


Figure 3.1: Illustration of the reflected and transmitted waves produced by an acoustic wave incident across a boundary between two media. Each boundary has distinct sound speeds ( $c$ ) and densities ( $\rho$ ). A portion of the wave is reflected at the angle of incidence ( $\theta_1$ ), and a portion is transmitted at the transmission angle, ( $\theta_2$ ).

Reflections produce multipath effects, illustrated in Figure 3.2. The difference in path length causes the wave fronts to differ in phase, causing constructive and destructive interference. Waves that are in phase will add constructively, while waves that are half-wavelengths out of phase will become vanishingly small.

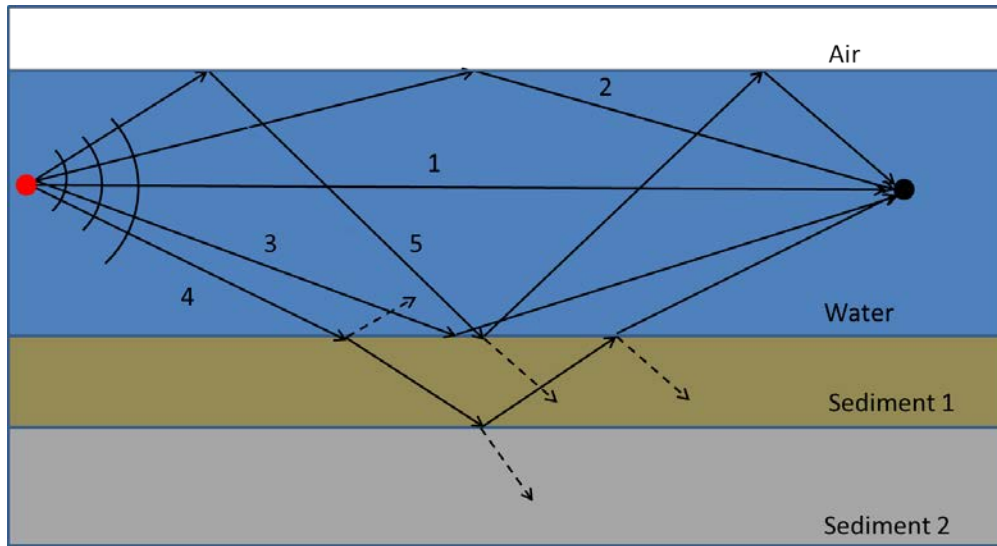


Figure 3.2: Possible multipath interactions between an arbitrary source and receiver. Illustrated are 1) the direct path, 2) the air-water interface reflected path, 3) the water-sediment reflected path, 4) the path transmitted through sediment 1 and reflected from sediment 2, and 5) the water-air, water-sediment, and water-air reflected path. The dotted arrows highlight the reflected or transmitted portion of the waveform that does not reach the receiver.

TL characterizes the reduction in sound levels from the source, and is typically expressed in decibels (dB). TL results from two primary factors: spreading loss and sediment attenuation. If an acoustic source is able to propagate freely into space, the acoustic energy will expand into the area of a sphere, and the source will experience spherical spreading. Conversely, a source between two perfectly reflecting parallel planes will only expand into the area of a cylinder and experience cylindrical spreading. In spherical spreading, TL is proportional to the inverse of the range squared, and in cylindrical spreading; it is proportional to only the inverse of the range.

In the shallow water case, the sound source is bounded by a perfectly reflecting plane (air-water) and lossy, reflective sediment layers. While the attenuation of sound in water is considered negligible, the attenuation in the sediment is not, and interactions with the sediment result in additional losses. For example, in Figure 3.2 before the sound reaches the receiver by path 4, it has experienced losses from transitioning to sediment 1, traveling through sediment 1, reflecting with sediment 2, and transitioning again to the water column. This is critical for an intuitive understanding of the sound attenuation predicted by the model. For example, shallower bathymetry results in increased reflections on the sediment-water interface and therefore greater loss.

An attempt has been made to amalgamate the various sources of TL into a simple model, known as the practical spreading model (PSM) (ICF 2009), which is currently used by the California Department of Transportation. The PSM simply computes the sound level by subtracting the scaled logarithm of range from an assumed source level,

$$LVL = SRCLVL - F \log r \quad (3.5)$$

Here LVL is the sound level at range  $r$ , SRCLVL is the assumed source level, and  $F$  is an attenuation factor that is allowed to vary from 5 to 30. This method has a number of problems. First, it assumes an environment that is homogeneous and axisymmetric, when in reality variations in sediment composition and bathymetry can significantly affect sound levels. The second problem is that SRCLVL and  $F$  cannot be trivially obtained, and must be determined by fitting acoustic data at several ranges. An example of PSM solutions is shown in Figure 3.3. There smooth curves can be seen that vary greatly depending on the choice of  $F$  parameter.

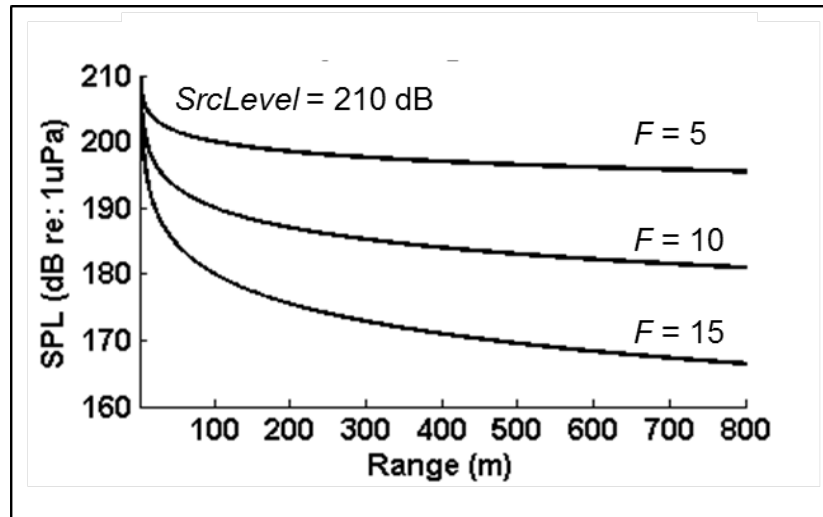


Figure 3.3: Practical spreading model solutions for  $F$  parameters of 5, 10, and 15 with a source level of 210 dB.

### 3.2 PARABOLIC EQUATION (PE) PROPAGATION

The PE method was chosen to compute physics based wave propagation because the method is well suited to calculate propagation in range-dependent and arbitrarily complex environments. Furthermore, the method was chosen because it is suitable for low frequency calculations, (below approximately 3000 Hz) where most pile driving energy is contained (*Stockham et al. 2010*). Computation of PE solutions was done using a mature and publicly available PE code, the RAM-PE (*Collins 1993*). The RAM-PE was originally developed for application to problems in sonar, and calculates the frequency dependent wave propagation through a two-dimensional geometry, shown in Figure 3.4. There, TL from a 1500Hz source is shown in range and depth propagated through multiple sediment layers and the water column. The bottom layer is an attenuation layer to prevent artificial reflections from returning into the simulation area.

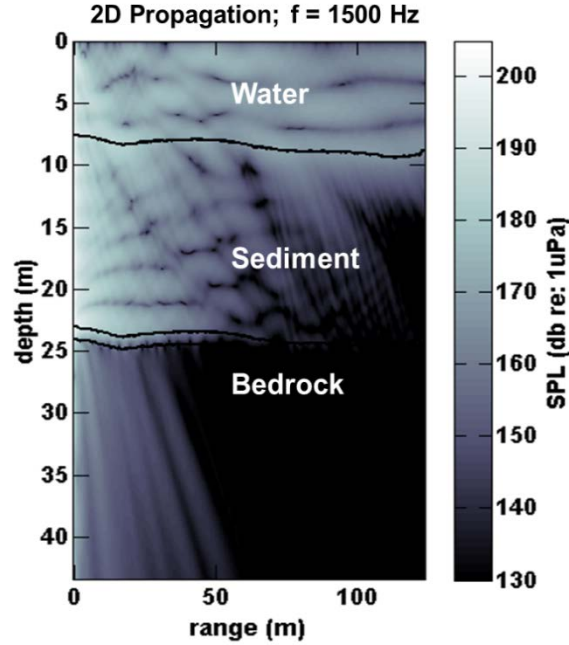


Figure 3.4: Example RAM-PE solution. SPL is plotted as a function of range and depth through multiple sediment layers.

The RAM-PE calculates propagation by solving the two-dimensional acoustic wave equation,

$$\frac{\delta^2 p}{\delta r^2} + \rho \frac{\delta}{\delta z} \left( \frac{1}{\rho} \frac{\delta p}{\delta z} \right) + k^2 p = 0 \quad (3.6)$$

where  $p$  is the acoustic pressure,  $\rho$  is the density,  $z$  is the receiver depth,  $r$  is the receiver range, and  $k$  is the wave number,  $k = \frac{2\pi}{\lambda}$ , where  $\lambda$  is the wavelength in the medium at the current range and depth. The solutions to this expression are Green's functions, which solve (3.6) for a given set of boundary conditions and inhomogeneities in the simulation environment. The Greens function is two-dimensional in range and depth, and frequency dependent,  $G(r, z, f)$ .

In the absence of environmental inhomogeneities and boundaries, (3.6) is solved by the free space point source,

$$G(r, z, f) = \frac{\exp(-ikr(r^2 + z^2)^2)}{(r^2 + z^2)^2} \quad (3.7)$$

The RAM-PE simplifies the wave equation by factoring (3.6) into a parabolic form, applying the assumption that forward energy dominates, and calculating solutions to the forward component of the wave equation,

$$\frac{\delta p}{\delta r} = ik_0(1 + X)^2 p \quad (3.8)$$

Here  $\square_0 = \frac{\omega}{v}$ , where  $\omega$  is the angular simulation frequency and  $\square$  is the representative phase speed. The operator  $X$  assures that (3.8) is satisfied for the given environmental boundary conditions and inhomogeneities,

$$X = k_0^{-2} \left( \rho \frac{\delta}{\delta z} \frac{1}{\rho} \frac{\delta}{\delta z} + k^2 - k_0^2 \right) \quad (3.9)$$

RAM solves (3.8) using a recursive relationship that calculates range dependent solutions based on a  $q$  term rational approximation,

$$G(\mathbf{r} + \Delta \mathbf{r}, \mathbf{z}, f) = e^{ik\Delta r} \prod_{q=1}^Q \frac{1 + C_{q,Q} X}{1 + B_{q,Q}} \rho(\mathbf{r}, \mathbf{z}) \quad (3.10)$$

where  $C_{q,Q}$  and  $B_{q,Q}$  are Padé series coefficients.

The initial fields (those fields at the first range step) are calculated using the self-starter, which calculates a particular solution to (3.6),

$$\frac{\delta \rho}{\delta r^2} + \rho \frac{\delta}{\delta z} \left( \frac{1}{\rho} \frac{\delta \rho}{\delta z} \right) + k^2 \rho = 2i\delta(z - z_0) \quad (3.11)$$

where  $z_0$  is the source depth. It is solved by,

$$G(\mathbf{r}_0, \mathbf{z}, f) = \frac{\exp(ik_0 r_0 (1 + X)^{1/2})}{k_0^{1/2} (1 + X)^{1/4}} \delta(z - z_0) \quad (3.12)$$

The resulting two-dimensional greens function solutions give the complex pressure fields in the specified environment, as produced by a 1  $\mu$ Pa source. The implementation and problem specific optimization of the RAM-PE are discussed in the appendices.

### 3.3 FREQUENCY SYNTHESIS

While the propagation model calculates a single frequency solution, broadband spectral and time domain analysis are of primary concern. Computing Green's function solutions over a broad band produces a two-dimensional frequency domain solution demarcated,  $S(\mathbf{r}, \mathbf{z}, f)$ . A time domain solution was obtained by synthesis of the many frequency domain components and carried out with the inverse discrete Fourier transform (DFT),

$$s_n(\mathbf{r}, \mathbf{z}, \eta) = \frac{2}{NT} \text{Re} \left\{ \sum_N S_n(\mathbf{r}, \mathbf{z}, n) e^{2n\frac{\eta}{N}} \right\} \quad (3.13)$$

where  $N$  is the total number of points in the transform,  $n$  is the  $n^{\text{th}}$  frequency domain sample, and  $\eta$  is the  $\eta^{\text{th}}$  time domain sample. Since the negative frequency components are not computed, the solution is multiplied by a factor of two, and the real part of the solution is taken. The resolution in the time domain is,

$$\Delta t = \frac{1}{N\Delta f} \quad (3.14)$$

where  $\Delta f$  is the frequency resolution. The time axis corresponding to the  $\eta^{\text{th}}$  bin is,

$$\mathbf{t} = [\Delta t, 2\Delta t, 3\Delta t, \dots, N\Delta t] \quad (3.15)$$

Computational efficiency is improved by selecting broadband parameters that accommodate the requirements of a robust model, but do not require more calculations than are needed. To this end, frequency domain parameters are chosen to accommodate the necessary time domain period as well as the relatively low frequency limitations of PE modeling.

The frequency resolution was chosen to create a time period sufficient for time domain propagation to the extent of the simulation range. That is, sufficient time so that the source function solution can propagate the length of the simulation area. This is based on the water column waveguide group velocity,

$$v_g = c_w \sqrt{1 - \left(\frac{\omega_0}{\omega}\right)^2} \quad (3.16)$$

where  $\omega$  is the maximum simulation angular frequency and  $\omega_0$  is the waveguide cutoff frequency. The cutoff frequency for the first mode is,

$$\omega_0 = 2\pi \frac{c_w}{2D} \quad (3.17)$$

where  $c_w$  is the speed of sound in water and  $D$  is the average depth of the water column. The necessary frequency resolution is,

$$\Delta f = \frac{v_g}{R_{max}} \quad (3.18)$$

where  $R_{max}$  is the maximum range of the simulation. For a maximum observation range of 800 meters, the frequency step is approximately 1.5 Hz.

The bandwidth is chosen to provide the greatest computational efficiency while still capturing most of the signal energy. This is done by spectral analysis of a close range, empirically observed pile driving waveform. An appropriate bandwidth is selected by comparing the sum of the energy spectral density (ESD) in the full spectrum of the close range observed signal, to that of the observed signal after a low pass filter has been applied. The percentage of the total signal energy in the truncated simulation is given by the fraction of the summed ESD,

$$B = \frac{\sum ESD_{obs}}{\sum ESD_{truncated}} \quad (3.19)$$

where  $ESD_{obs}$  is the ESD summed over all bins in the observed measurement,  $ESD_{truncated}$  is the bandwidth truncated ESD, and B is the ratio between the two. For the 24 inch piles in this work, a maximum frequency of 2600 Hz contained 97 percent of the total signal energy, while for the 48 inch piles; a maximum frequency of only 2100 Hz was needed to capture the same percentage of energy.

### 3.4 GEOACOUSTIC MODEL

PE modeling allows the use of range dependent bathymetry and geoacoustic parameters. For each range step, propagation is calculated based on the bathymetry and three geophysical parameters for each sediment layer: density, sound speed, and attenuation. These parameters define each sediment layer and can be arbitrary updated in range and depth. Geophysical parameters were based upon boring logs and laboratory analysis of coring samples (*Kinsler et al. 2000, CRC 2012a, CRC 2012b*) taken at several locations in the Columbia River. Measured parameters that influenced the formulation of the geophysical model were grain size, porosity, and sound speed. An example coring sample taken from the boring studies is shown in Figure 3.5.

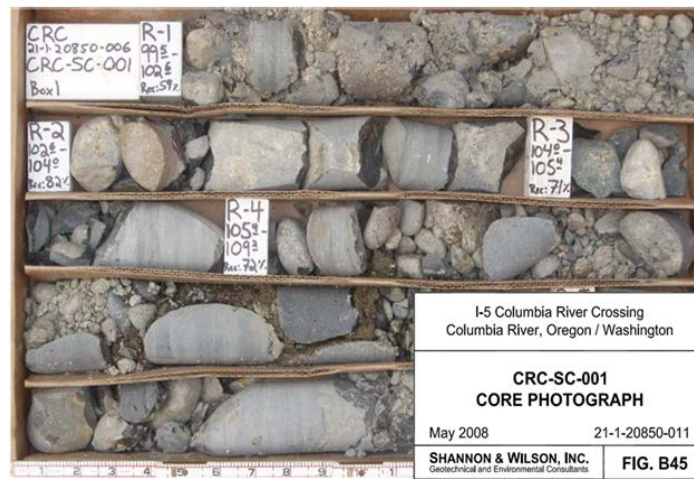


Figure 3.5: Example coring sample taken of the Troutdale Formation under the Columbia River.

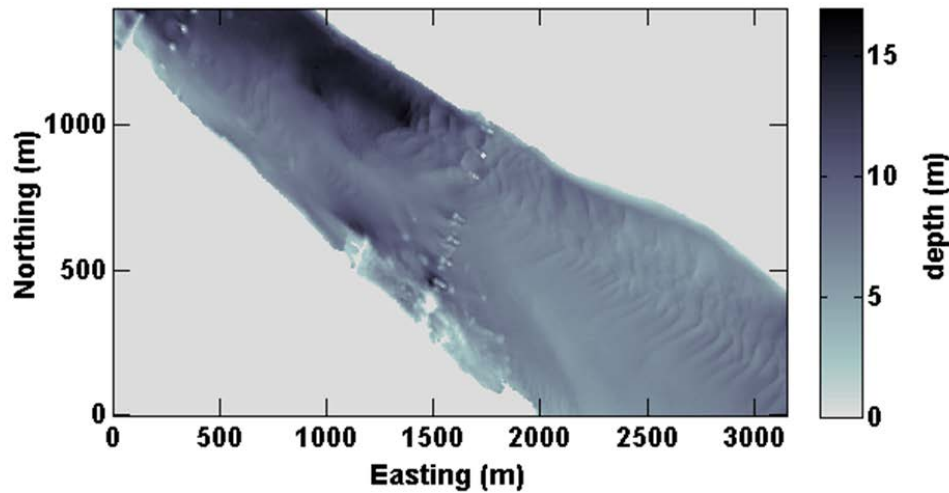


Figure 3.6: Columbia River Bathymetry between Portland, OR and Vancouver WA, obtained from NOAA fathometer measurements. The gray scale represents river depth and the areas of zero depth at figure center correspond to the existing I5 span.

The bathymetry shown Figure 3.6 was taken from NOAA fathometer measurements, and shows a shallow, inhomogeneous river environment, with main channel depths from 6 to 17 meters. Transects of this bathymetry were taken and used directly in the model.

The boring records indicate three main sediment layers (Figure 3.7): a top layer of medium grained sand, a thin medium gravel layer, and a dense cobblestone bedrock layer, known as the Troutdale Formation. Each of these sediment layers had uniquely defined geophysical parameters shown in Table 3.1. Identical parameters were used for each layer in all of the sites that were considered, although the layer depths were varied for each location based on the boring records. The primary sediment layer variation was in the thickness of the medium sand layer, which varied significantly between the North and South Riversides. On the North riverside, it is as thin as 12.5 meters below the mud line, whereas at the south riverside, it is as thick as 60 meters. This variation results in the depth of the highly reflective Troutdale Formation, and therefore its effect on sound levels, to vary significantly across the width of the River.

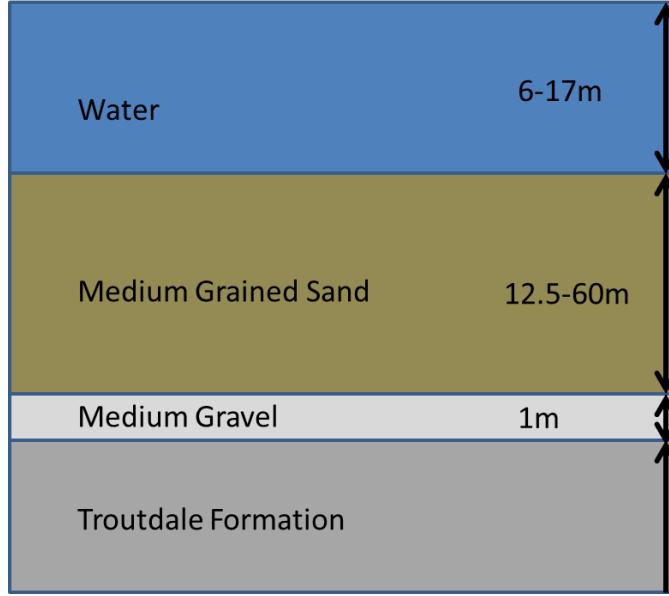


Figure 3.7: The sediment layers used in the model. The arrows on the right of the figure indicate the variability in each sediment layer. The Troutdale Formation represents the acoustic basement and is effectively of infinite depth.

**Table 3.1: Summary of Geoacoustic Parameters**

Material	Density (g/cc)	Attenuation (dB/λ)	Approx. Sound Speed (m/s)
Sand	1.84	0.88	1500
Gravel	2.15	0.88-0.75 (Interpolated)	1550-2856 (Interpolated)
Troutdale Formation	2.50	0.75	2856

Sediment density was obtained using the laboratory measurements, particularly the porosity, or water content. This was used in conjunction with the bulk density (based on the sediment description) to derive the density,

$$\rho_s = \epsilon \rho_w + (1 - \epsilon) \rho_{sb} \quad (3.20)$$

where  $\epsilon$  is the sediment porosity,  $\rho_s$  is the sediment density, and  $\rho_{sb}$  is the bulk sediment density. Sediment attenuation is based on the viscoelastic model of Hamilton (1980) (DEA 2011). This model describes sediment attenuation that varies linearly with frequency,

$$\alpha = k_p f \quad (3.21)$$

where  $\alpha$  is the attenuation in  $\frac{\text{dB}}{\lambda}$  and  $k_p$  is the loss parameter. The loss parameters used were taken from a table in the APL-UW High Frequency Ocean Environment Acoustic Models Handbook (APL-UW 1994). Values were chosen by matching the sediment description, grain size and ratios of density and velocity from the boring studies and equation (3.21), to a loss parameter from the table.

Sound speed profiles were measured in 6 of the boring measurements, and resulted in sound speed curves such as those in Figure 3.8. Values from these curves were used in the computational model, and for depths where values were not explicitly defined, approximate values were used based on these curves (Table 3.1).

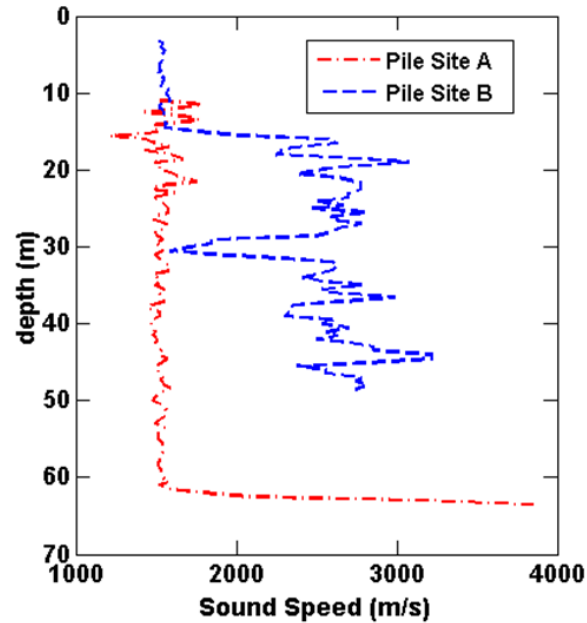


Figure 3.8: Sound speed profiles for sites A and B. The lower sound speed regions at shallow depth correspond to the sand layer, the rapid transition corresponds to the narrow gravel layer, and the high sound speed region corresponds to the Troutdale Formation.



## 4.0 MODELING THE PILE DRIVING SOURCE

The impact between the hammer and pile causes a deformation in the pile material, which results in the initial pressure fields of the pile driving impact. The empirical and FDTD source models presented below provide contrasting models of this deformation, which are discussed at the end of this chapter and quantified in chapter 5. In both cases, the source functions are coupled into the propagation model to produce a two-dimensional broadband simulation. These Green's function solutions are demarcated  $S_{\text{emp}}(r, z, f)$  for the empirical source model, and  $S_{\text{FDTD}}(r, z, f)$  for the FDTD source model. Results using both source models can be processed identically and the subscript is kept only to specify the origin of the simulation.

### 4.1 EMPIRICAL SOURCE MODEL

The empirical source model is based upon the work of Reinhall and Dahl (2011), and is a time and spatially variant model of pile deformation that incorporates information from a close range, empirically observed waveform to assure source agreement in spectral, time extent, and total energy characteristics. The model accounts for the pile driving impact with the assumption that the vast majority of the energy radiated into the environment results from an impulse bulge traveling through the pile. This bulge travels at the speed of sound in steel, reflects at the ends of the pile, and is attenuated at the reflection between the pile and sediment. Since the speed of sound in the pile ( $c_p = 5100$  ms) is much greater than that in the environment ( $c_w = 1447$  ms), energy is radiated in conical arrivals of incidence angle,

$$\varphi = \arcsin\left(\frac{c_p}{c_s}\right) \quad (4.1)$$

where  $c_p$  is the speed of sound in the pile and  $c_s$  is the speed of sound in the sediment. Also,  $c_w$ , the sound speed in water, is substituted in (4.1) for  $c_w$  if the bulge is currently in the water column rather than then sediment.

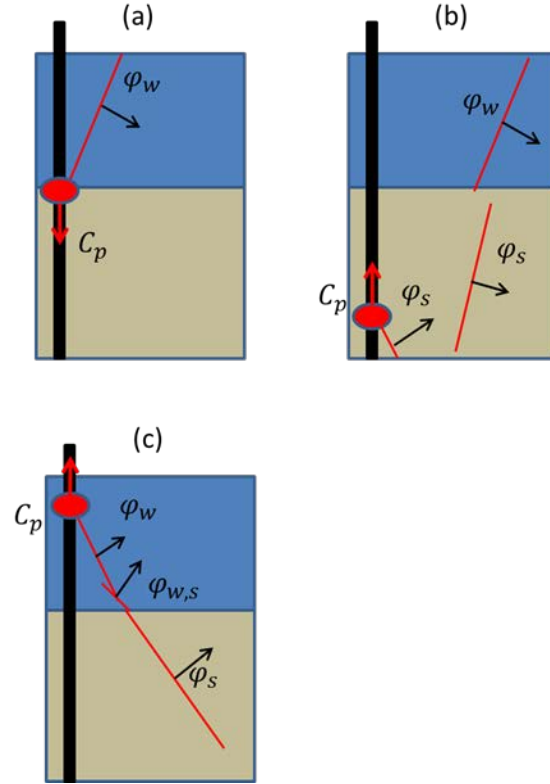


Figure 4.1: The arrivals of the empirical source model. Panels (a), (b), and (c) show the bulge traveling through the pile and the emitted arrivals at progressively later times.  $c_p$  is the speed of sound in the pile and  $\varphi_w$  is the arrival angle in the water,  $\varphi_s$  is the arrival angle in the sediment, and  $\varphi_{w,s}$  is the angle of the arrival that originated in the sediment and transitioned to the water.

At each instance of the bulge traversing the pile, a conical arrival is generated, shown in Figure 4.1. Panel (a) shows the first arrival, shortly after the hammer impact. Panel (b) shows the first arrival in the sediment, with conical waves traveling at slightly different angles, based in the difference between water and sediment sound speed. Also, the beginning of the second arrival can be seen, as the bulge has reflected at the bottom of the pile and is now traveling up the pile. Panel (c) shows the full second arrival, with the conical waves described in Panel (b), as well as a small wave at a third angle, which originated in the sediment and has transitioned into the water. The bulge continues to reflect at the top and bottom of the pile and produce similar arrivals, until it has been completely attenuated. The bulge is considered to be of uniform amplitude while traversing the pile, and is attenuated at the pile-sediment reflection.

The source is implemented by forming each  $m^{\text{th}}$  conical arrival separately as an array of point sources solutions, invoking Huygens' Principle. The expression for the  $j^{\text{th}}$  depth point source is,

$$s_{emp,m,j}(\mathbf{r}, \mathbf{z}, \mathbf{f}) = G(\mathbf{r}, \mathbf{z}, \mathbf{f})\gamma(\mathbf{f})e^{-i2\pi\mathbf{f}\tau_{m,j}} \quad (4.2)$$

where the emp subscript denotes the empirical model,  $G(\mathbf{r}, \mathbf{z}, \mathbf{f})$  is the broadband point source solution calculated by the RAM-PE at each frequency and  $\gamma(\mathbf{f})$  is a spectral weighting function.

The exponential term is a depth dependent time delay of  $\tau_{m,j}$  that steers the arrival to the proper incidence angle, (equation 4.1) by the shift theorem (*Ifeachor and Jervis 1993*). The time delay is the time required for the bulge to reach the  $j^{\text{th}}$  depth point source on the pile and depends on the dimensions of the pile. The delays  $\tau_{m,j}$  for the first four  $m^{\text{th}}$  arrivals at the  $j^{\text{th}}$  source depth are,

$$\tau_{1,j} = \frac{c_p}{d_j}, \quad \tau_{2,j} = \frac{2p_{wl}-d_j}{c_p}, \quad \tau_{3,j} = \frac{2p_{wl}+d_j}{c_p}, \quad \tau_{4,j} = \frac{4p_{wl}-d_j}{c_p} \quad (4.3)$$

where  $d_j$  is the depth of the  $j^{\text{th}}$  point source.

Summing over all source depths results in the conical wave of the  $m^{\text{th}}$  arrival,

$$S_{emp,m}(\mathbf{r}, z, f) = \frac{1}{J} \sum_{j=1}^J s_{emp,m,j}(\mathbf{r}, z, f) \quad (4.4)$$

where  $J$  is the total number of point sources. The full simulation is computed by summing over all arrivals, accounting for bulge attenuation and applying the energy matching constant.

$$S_{emp}(\mathbf{r}, z, f) = C \sum_{m=1}^M (-1)^{m+1} K_m S_{emp,m}(\mathbf{r}, z, f) \quad (4.5)$$

Here  $C$  is the energy matching constant, and  $K_m$  is a constant parameter which models the attenuation of the bulge at each arrival.

The empirical parameters,  $\gamma(f)$ ,  $C$ , and  $K_m$ , are derived from a close range, empirically observed waveform, resulting from a pile driving event. For the derivation of the spectral weight function and attenuation constant, it is useful to isolate the arrivals from the empirical waveform. Arrivals are isolated by determining the time separating arrivals, which depends on motion of the bulge through the pile, and is determined by a geometrical argument. The length of time between an odd and even numbered arrival is,

$$\Delta T_{Odd \rightarrow Even} = \frac{2(p_{wl} - z)}{c_p} \quad (4.6)$$

where  $z$  is the receiver depth. This corresponds to the transition between arrivals where the bulge reflects at the bottom of the pile. The length of time from even to odd arrivals is,

$$\Delta T_{Even \rightarrow Odd} = \frac{2[(p_l - p_{wl}) + z]}{c_p} \quad (4.7)$$

which corresponds to the arrival transition where the bulge reflects at the top of the pile. These arrival times are superimposed on an empirical waveform in Figure 4.2. Since the receiver for this waveform is positioned well above the middle point of pile, the odd arrivals occupy considerably more time. Also, distinct peaks cannot be seen as clearly for the even arrivals because these arrivals have traveled through the sediment before reaching the receiver.

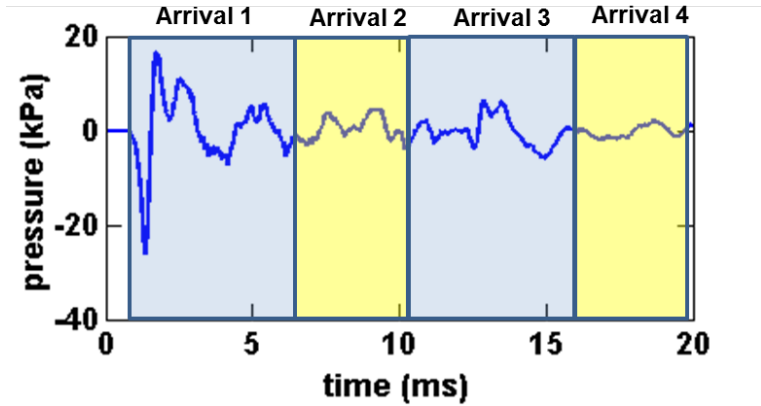


Figure 4.2: Empirically observed pile driving waveform resulting from a 10 meter observation of pile B1. Receiver is at 3.75 meter depth.

The spectral weighting function,  $\gamma(f)$  is defined as the normalized Fourier transform magnitude of the first arrival, taken from a close-range observed waveform. Figure 4.3 shows an example spectral weight function, originating from pile B1. It is used to weight the magnitude of each frequency dependent simulation such that the simulated and observed spectra match at close range.

The value of  $\gamma(f)$  is calculated as follows. The first arrival is isolated by calculating the corresponding time from equation 4.6. All samples at times not corresponding to the first arrival are discarded. An isolated first arrival is shown in Figure 4.4. The first arrival is then converted to the frequency domain using the DFT, normalized, and truncated to the bandwidth of the numerical simulation. Finally, a gentle 0.015 factor Tukey window (*Ifeachor and Jervis 1993*) was applied to reduce any ringing effects in the time domain synthesis.

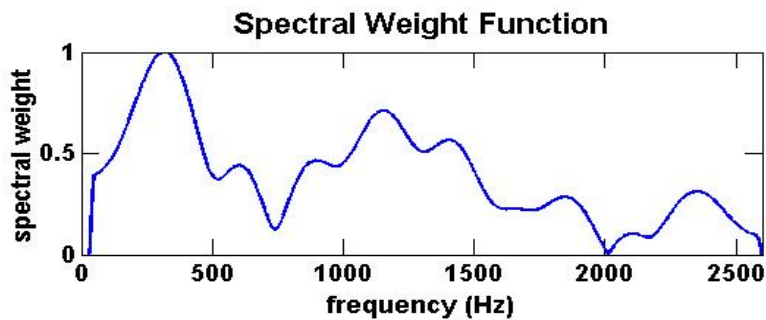


Figure 4.3: Example spectral weight function formulated from an empirical observation of a hammer impact on pile B1

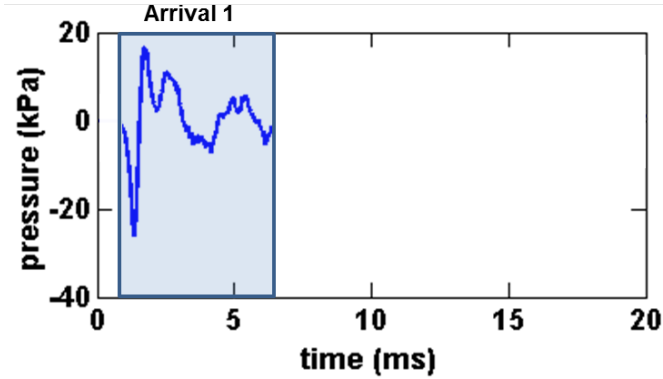


Figure 4.4: First arrival isolated from the empirical waveform. Samples not corresponding to the first arrival have been discarded.

The attenuation parameter  $K_m$  depends exponentially on the arrival number  $m$ ,

$$K_m = \begin{cases} \kappa^{m-2}, & \text{if } m = 1, 3, 5, \dots \\ \kappa^{m-1}, & \text{if } m = 2, 4, 6, \dots \end{cases} \quad (4.8)$$

where  $\kappa$  is a real number between zero and one, and is equal to the amplitude ratio of the first and third arrival maximum amplitudes. The energy matching constant  $C$  is chosen such that the sum of the ESD of the simulated spectrum matches the sum of the ESD of the observed spectrum, at the observation point, over the simulated bandwidth. It is a function of the observed and simulated signals,

$$C = \frac{\sum ESD_{Observed}}{\sum ESD_{Simulated}} \quad (4.9)$$

## 4.2 FDTD SOURCE MODEL

Under the ODOT sponsored program that supported this work, Shahab and Hastings at GTech worked under subcontract with the NEAR-Lab to develop a rigorous and purely computational model of the pile deformation. Their work culminated in the development of an FDTD model of deformation at discrete elements along the pile surface (*Shahab and Hastings 2011*). The model uses several parameters including the full geacoustic model, the pile material and dimensions, the cap placed between the pile and hammer, and the force waveform between the hammer and pile. The model computes the deformation of the pile by solving the equations of motion of a cylindrical shell with an FDTD (*Edmondson 1970, Goldberg and Korman 1974, Junger, 1997, and Warburton 1961*) method. Solutions were provided by the GTech, which was only able to provide a preliminary source for pile B1 at the time of this writing.

The coupling of the FDTD model into the propagation model is described in Figure 4.5. The FDTD model calculates pile deformation as the particle velocity of  $J$  discrete cylindrical shells. Since the RAM-PE calculates the solution to a spherical point source, the cylindrical particle velocity solutions are coupled into the propagation model by formulation of the simple source

pressure field (Kinsler *et al.* 2000), which is convolved with the propagation model point source array (Kinsler *et al.* 2000).

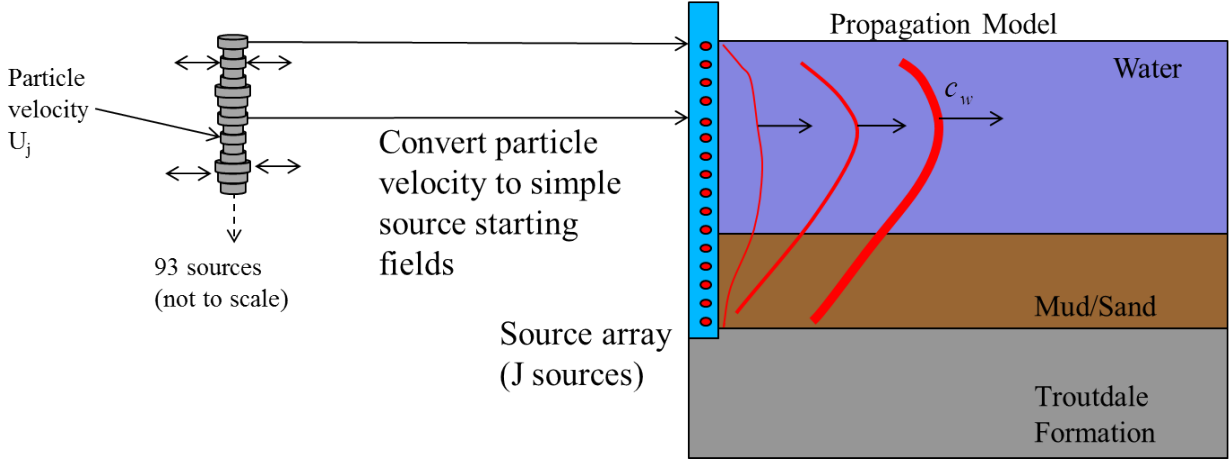


Figure 4.5: Illustration of the FDTD Source Model, and the coupling into the propagation model. The cylindrical shells on the left represent the nodal particle velocity solutions of radius  $a$  and height  $dz$ . The  $N$  particle velocity nodes are converted to  $N$  simple sources and convolved with the RAM-PE Green's functions solutions, represented by red dots at right.

The pressure field of the  $j$ th simple source is,

$$p_j(\mathbf{r}, t, f) = \zeta_j \left( \frac{Q}{4\pi a \xi} \right) e^{i[\omega t - k(\xi - a)]} \quad (4.10)$$

where  $a$  is the simple source radius,  $\xi$  is the distance from the origin, and  $\zeta_j$  is the specific acoustic impedance of a sphere,

$$\zeta_j(f) = \rho_j c_j \frac{[k(f)\xi]^2}{1 + [k(f)r]^2} + i\rho_j c_j \frac{k(f)\xi}{1 + [k(f)\xi]^2} \quad (4.11)$$

As with the empirical source model,  $j$  indexes the  $j$ th source depth,  $\rho_j$  and  $c_j$  are the density and sound speed surrounding the  $j$ th point source and  $Q_j$  is the source strength of a moving cylindrical shell,

$$Q_j = 2\pi a U_j(f) dz \quad (4.12)$$

Here,  $dz$  is the node depth spacing, and  $U_j(f)$  is the discrete Fourier transform of the time domain particle velocity. Combining (4.10), (4.11), and (4.12), then imposing the conditions that  $t = 0$  and  $\xi = a$  results in the starting pressure fields for a single node,

$$p_j(f) = \zeta_j(f) \frac{U_j(f) dz}{2a} \quad (4.13)$$

The starting pressure field is propagated by convolution with the specific Green's function, calculated by the RAM-PE,

$$P_j(\mathbf{r}, \mathbf{z}, f) = p_j(f)G_j(\mathbf{r}, \mathbf{z}, f) \quad (4.14)$$

The total Green's function is the sum of the propagated simple sources,

$$S_{FDTD}(\mathbf{r}, \mathbf{z}, f) = \sum_{j=1}^J P_j(\mathbf{r}, \mathbf{z}, f), \quad (4.15)$$

where the FDTD subscript denotes the FDTD source model.

The simple source formulation derived above is dependent upon the pressure at the uniformly vibrating surface of the modeled source being approximately equal to the pressure that would be produced at the surface of an identically vibrating sphere. For arbitrary sources, this assumption requires that  $ka \ll 1$ . While this condition is not satisfied at the upper frequencies of the model, it was shown to be valid for the cylindrical source in question.

The pressure field of an arbitrary source is the particle velocity  $u$  multiplied by the acoustic impedance  $\zeta$ ,

$$p = u\zeta \quad (4.16)$$

Therefore, for identical particle velocities, the ratio of pressure is the ratio of the specific acoustic impedances. Using (4.11) and the specific acoustic impedance of a cylinder,

$$\zeta_{cylinder} = \frac{i\rho_0 c H_0^{(2)}(kr)}{H_1^{(2)}(kr)} \quad (4.17)$$

where  $H_0$  and  $H_1$  are Hankel functions of the first and second kind, the magnitude of the pressure ratio at the surface of the cylindrical shell and maximum frequency is given by,

$$\frac{|p_{sphere}|}{|p_{cylinder}|} = \frac{\zeta_{sphere}}{\zeta_{cylinder}} \quad (4.18)$$

When evaluated at  $r = 0.609$  meters and  $f = 2600$  Hz, the ratio defined in (4.18) is 0.9952. Thus the approximation is accurate to less than one part in one hundred, and should be reasonable.

### 4.3 DISCUSSION

The empirical and FDTD source models are contrasting methods of accounting for the pile source and have different practical considerations for both implementation and sound level prediction. Due to the reliance upon an empirical measurement for the implementation of the empirical source model, this of course necessitates a suitable observation of a pile driving event, or at least a reference waveform from a similar pile type and environmental configuration. The FDTD source model does not have any such reliance but instead is dependent upon an accurate pile-hammer impact waveform and geoacoustic model.

Aside from the drawback that the empirical source model relies upon an observed waveform, simulated results produced by the empirical source model are assured good agreement in total energy, spectral, and time domain shape characteristics at the source due to this dependence. The empirical source model is also robust to uncertainty in the geoacoustic configuration directly surrounding the pile, as it is not derived based on knowledge of these parameters. Conversely the FDTD source as implemented in this work showed good agreement using just the geoacoustic survey work done leading up to construction. Furthermore, while the empirical source model provides a good match based on array measurements (*Reinhall and Dahl 2011*), the FDTD source model is a more fundamentally physics based model based on the vibration of a partially submerged cylinder, and could provide additional physical intuition.

For both the empirical and FDTD source models, the source functions were visualized using a short-range synthesis of the broadband RAM-PE solutions. In Figure 4.6 and Figure 4.7, the transmission loss is shown over a two-dimensional area, at time steps of 5, 10, 20 and 30 ms. In addition to illustration of the source functions, these plots verified that the intended source function was properly implemented. Proper implementation was verified by comparing the theoretical predictions from above to the simulated results, and also by verifying that the simulation was free of artifacts caused by improper implementation or lack of convergence.

In the visualization of the empirical source model in Figure 4.6, conical waves can be seen to radiate uniformly into the environment at the angles predicted by equation (4.1). This is contrasted by the visualization of the FDTD source model shown in Figure 4.7. For the first 10ms, very little sound is radiated into the environment. This corresponds to the period of time when the hammer is in contact with the pile, but the bulk of the force has not yet been applied. When the main force is applied, a conical wave is radiated at a similar incidence angle to the first arrival of the empirical model. However, after the first arrival, the modal response of the pile dominates, and the conical wave structure of the empirical model is no longer present.

Likely the most important distinction between the source models is the amount of energy radiated into the sediment. While the empirical source model radiates energy uniformly into the water column and sediment, the FDTD model radiates very little into the sediment. This is a topic that needs to be addressed in future research, and is of particular consequence to methods of attenuating the underwater sound. Typical methods of sound attenuation reduce only sound that has been emitted in the water column (*Stokes et al. 2010, Würsig et al. 2000*). The portion of sound produced in the water column as compared to in the sediment could have significant implications for the viability of such attenuation methods.

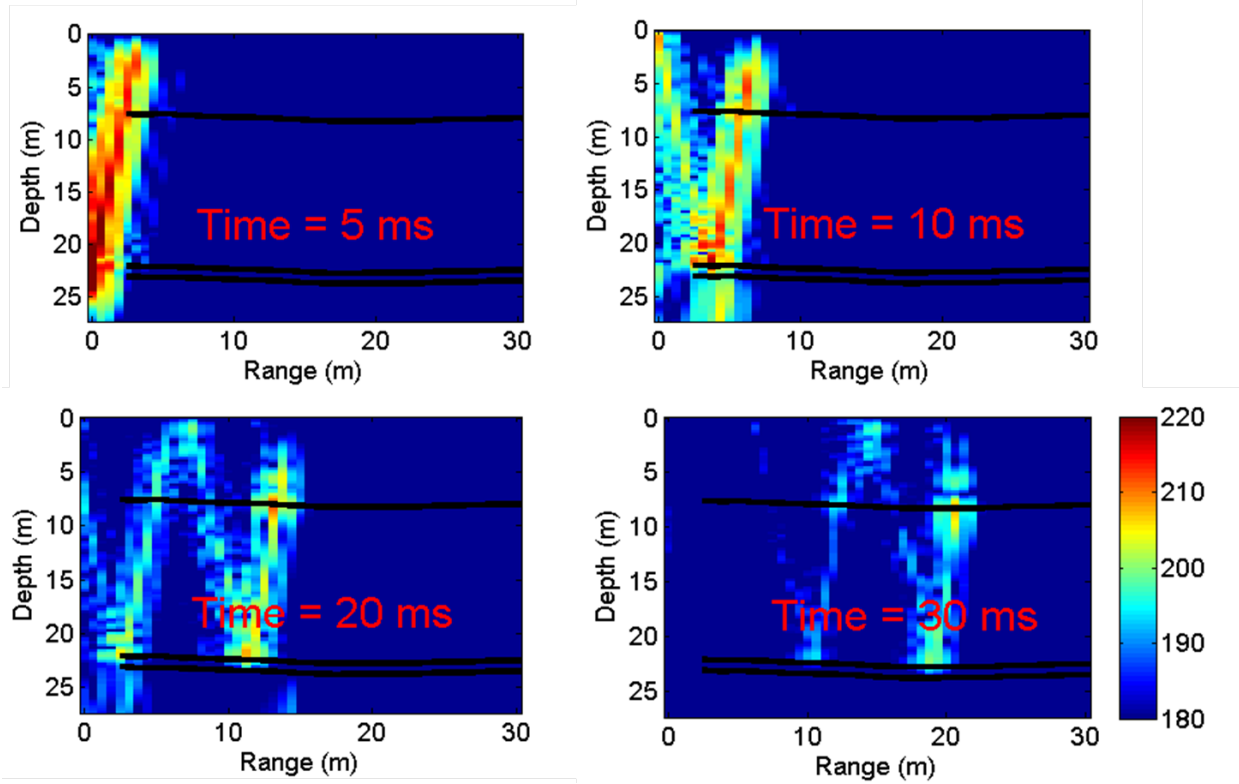


Figure 4.6: Short-range propagation still frames using the empirical source model to represent pile B1. The angled waves were emitted from the pile for a time period that included 4 arrivals. The black lines demarcate the sediment layer boundaries. The top layer is the water column, followed by sand, gravel and the Troutdale Formation, descending downward.

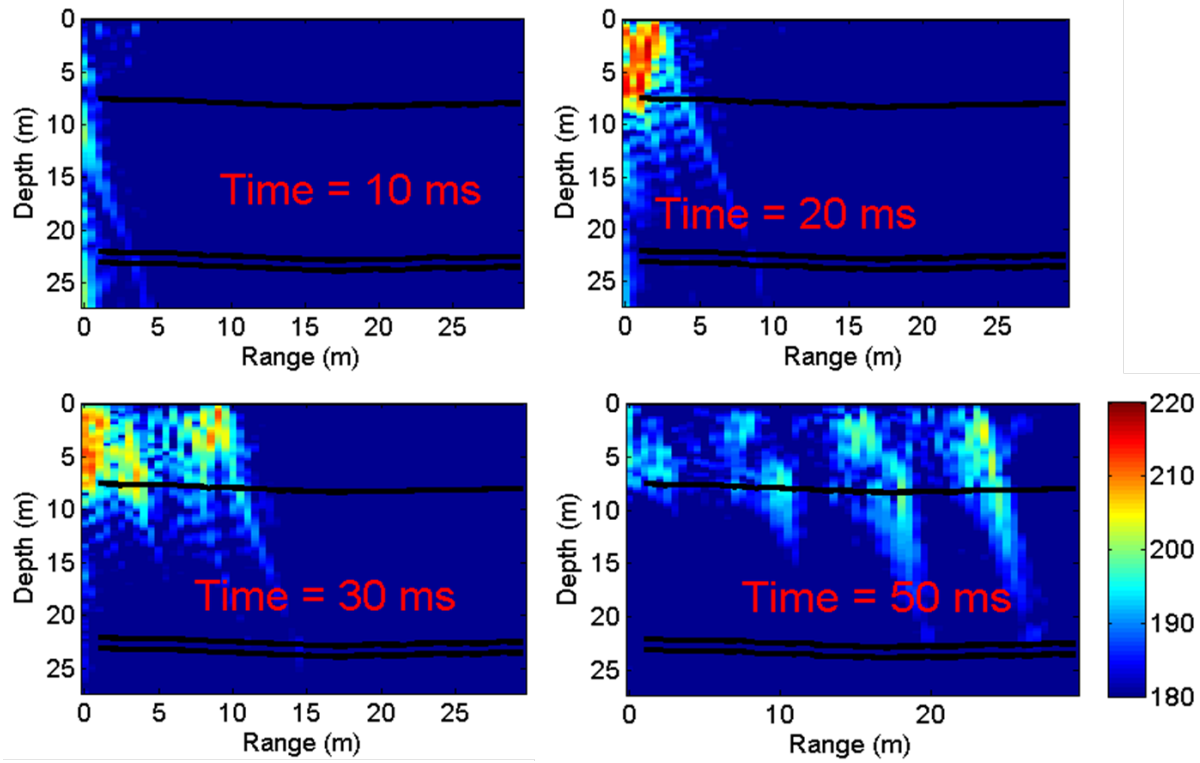


Figure 4.7: Short-range propagation still frames using the FDTD source model to represent pile B1. The lines demarcate the sediment layer boundaries. The top layer is the water column, followed by sand, gravel and the Troutdale Formation, descending downward.

## 5.0 MODEL VALIDATION

In this chapter the validity of the source models and propagation model are evaluated by comparisons with measured data in a variety of environmental conditions. Acoustic observations were taken of test pile operations in the Columbia River (*DEA 2011*) at several locations on both the north and south riversides. The simulated results correspond to two-dimensional (range, depth) simulations calculated along the path of acoustic observations, which use parameters corresponding to the pile types used in test pile operations and local geological configurations. These simulations model the acoustic propagation of sound from the test piles and are suitable for comparison directly with the acoustic observations. Comparisons are made in sound pressure level (SPL) power spectral density (PSD) and sound exposure level (SEL). Acoustic observations and model results are also compared to levels predicted by the practical spreading model.

### 5.1 EXPERIMENTAL DATA

Environmental monitoring of test pile operations in the Columbia River was done in February, 2011. The location of test pile operations corresponded to the Columbia River between Portland, OR, and Vancouver, WA, in the path of the proposed I5 span. In these tests, steel piles of 24 and 48 inch diameters were driven into both the north (Pile Site B) and south (Pile Site A) riversides, shown in Figure 5.1. On the north riverside, the 24 inch and 48 inch piles are labeled B1 and B2 respectively, and on the south riverside, they are labeled A1 and A3.

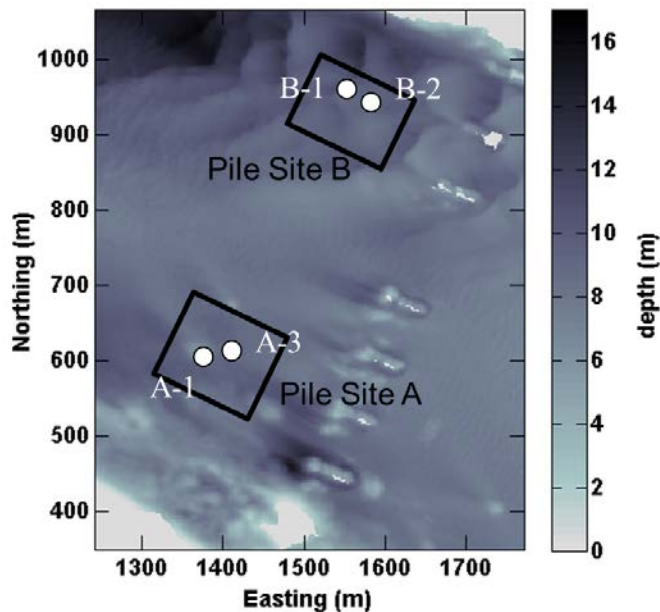


Figure 5.1: Test pile locations in pile sites A and B located in the path of the proposed new I5 span. Piles B1 and A1 are 24 inch diameter piles and Piles B2 and A3 are 48 inch diameter piles. Grayscale corresponds to water depth.

Acoustic observations were taken of these pile driving activities by the consulting firm David Evans and Associates of each pile at 5 locations, ranging from 10 to 800 meters. This provided 20 high quality measurements, spanning diverse ranges, variations in bathymetry, and pile types, for model comparisons (Figure 5.2).

At each monitoring location, the time domain waveforms were recorded several hammer impacts, shown in Figure 5.3 as SPL. Individual impacts were isolated using a threshold method, and were used to generate an ensemble average waveform, SEL, and PSD, shown in Figure 5.4. The PSD was calculated by the Welch method, using 2048 point segments and a Hamming window with the corresponding window correction factor applied. This specific analysis was chosen to match the analysis done by the David Evans and Associates engineers.

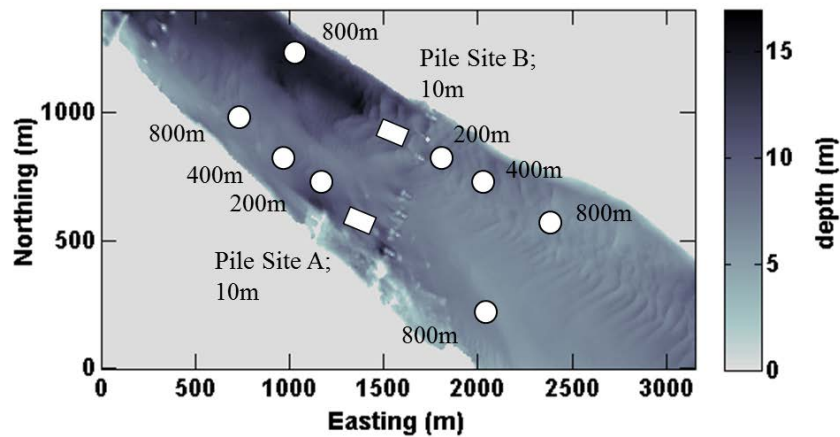


Figure 5.2: Test pile monitoring locations. Observations along the north riverside correspond to pile site B, and those along the south riverside correspond to pile site A. Grayscale corresponds to water depth.

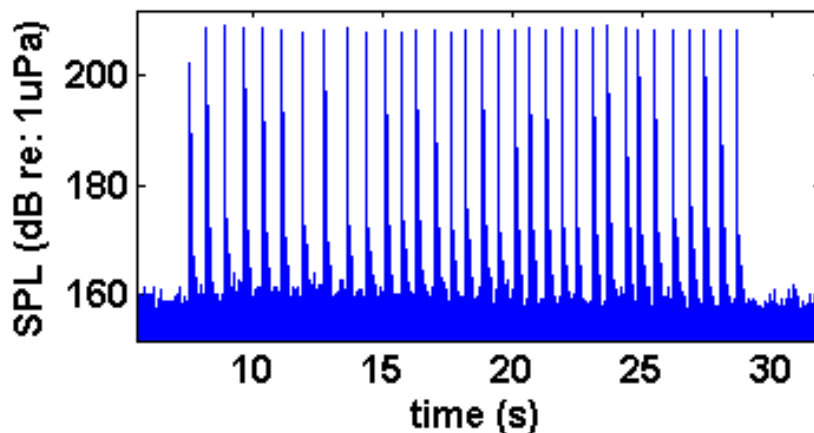


Figure 5.3: Data record of pile driving impacts on test pile B1 taken at 10m from the pile location. Impacts are shown as SPL.

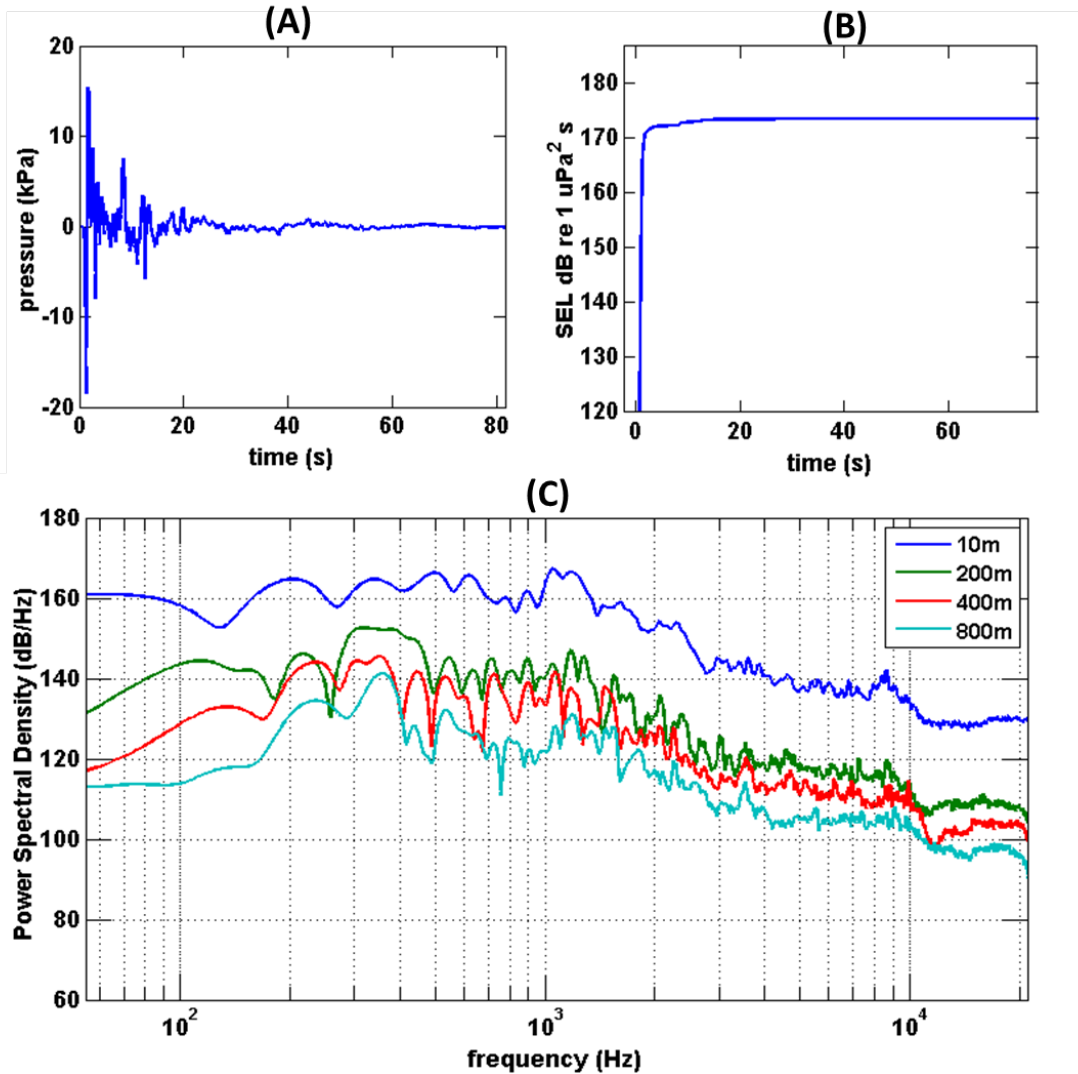


Figure 5.4: Example acoustic data from pile B1. Panel (A) shows the average time domain waveform from the 10 m monitoring location. Panel (B) shows the SEL computed from the waveform in Panel (A), and Panel (C) plots the PSD calculated from observations from 10 to 800 meters from the test pile site.

## 5.2 SIMULATION CONFIGURATION

The computational model was applied to replicate these acoustic observations such that the two could be compared for model validation. Simulations were computed along the paths of the acoustic observations and accounted for the corresponding bathymetry, geological configuration and test pile dimensions. The geoacoustic parameters from Section 3.4 were used with parameters that are specific to each test pile, summarized in Table 5.1. These parameters included the pile dimensions, sediment depths, and the empirically derived parameters used for the empirical source model. Also, the spectral weight functions for use with the empirical source model were derived from the 10 meters observations taken of each pile and are shown in Figure 5.5.

Examination of the parameters in Table 5.1 reveals some important distinctions between the test piles. The difference in Troutdale Formation depths between pile sites A and B highlights the variable geological configuration between the north and south riversides. Also note that the larger piles produce significantly higher sound levels, which is reflected in the higher empirical offset parameters needed to match simulation energy. Also, the larger piles tend to concentrate the acoustic energy in the lower frequency components, and therefore require lower maximum simulation frequencies to contain 97% of the impact energy. This concentration of energy at the low frequencies is further illustrated by the spectral weight functions in Figure 5.5.

**Table 5.1: Test Pile Model Parameters**

Pile	B1	B2	A1	A3
Diameter (in)	24	48	24	48
Length (m)	27.75	29.25	24.75	40
Wetted Length (m)	22.50	23.50	18.25	33.5
Gravel Depth (m)	14.5	14.5	60.0	60.0
Troutdale Formations Depth (m)	15.5	15.5	62.0	62.0
Empirical Offset (dB)	90.2	96.7	91.1	100.0
Attenuation Factor $K_m$	1/3	1/5	2/5	2/5
Maximum Frequency (Hz)	2600	2050	2600	2100

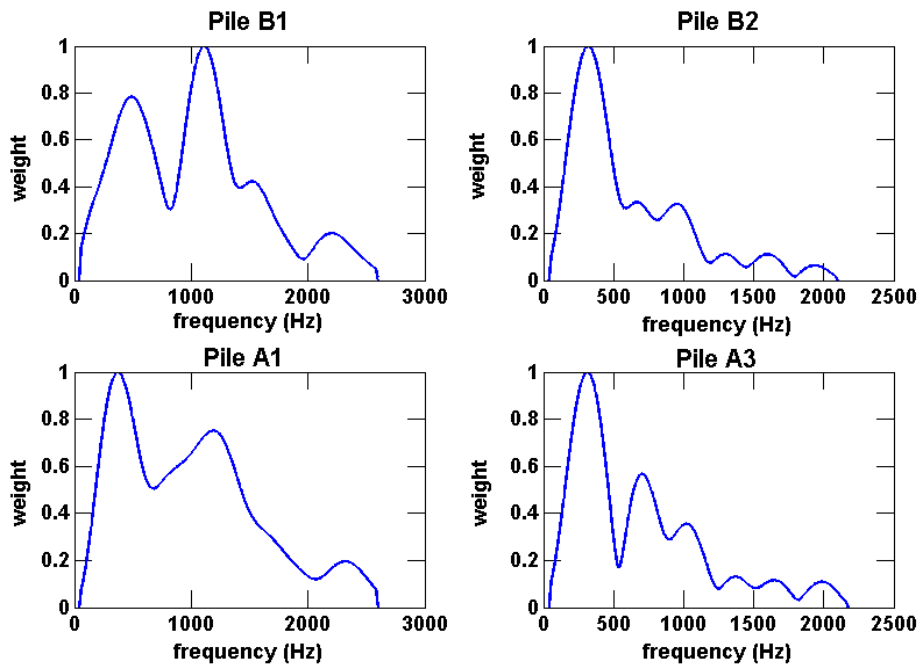


Figure 5.5: Spectral weight functions for each pile. All weight functions are derived from observations taken at 10 m from the corresponding test piles.

### 5.3 MEASUREMENT METRICS

The total Green's function propagation solutions for both source models,  $S_{\text{emp}}(r, z, f)$  and  $S_{\text{FDTD}}(r, z, f)$ , define the broadband complex pressure at each point in the simulation area. These results can be directly compared with the observed data using several frequency and time domain metrics, defined in this section.

Frequency domain analysis is performed by examination of the Power Spectral Density (PSD),

$$PSD = \frac{\nu}{L} \sum_{l=0}^{L-1} P_l(f) \quad (5.1)$$

where  $P_l(f)$  is the  $l$ th windowed periodogram and  $L$  is the total number of periodograms. Periodograms are obtained by first dividing the time domain waveform into  $L$  equal segments that overlap. The segments are then windowed and transformed to the frequency domain. The periodograms are calculated by computing the Energy Spectral Density (ESD) of the windowed and transformed segments,

$$ESD = S(r, z, f)^2 \quad (5.2)$$

The correction factor  $\nu$  is a constant that corrects for the energy lost by windowing,

$$\nu = \frac{1}{G} \sum_{g=0}^{G-1} w^2(g) \quad (5.3)$$

where  $w(g)$  is the  $g$ th window function bin, and  $G$  is the total number of points in the window. Note that for PSD analysis of the simulated data, a time domain waveform must be synthesized for application of the PSD algorithm.

In the time domain, data was analyzed in terms of Sound Pressure Level (SPL),

$$SPL = 10 \log_{10}(|s(r, z, t)|^2) \quad (5.4)$$

where SPL is relative to  $1 \mu\text{Pa}$  and has units of dB relative to  $1 \mu\text{Pa}$ , and Sound Exposure Level (SEL),

$$SEL = 10 \log_{10} \left( \sum_{k=1}^K |s_k(r, z, t)|^2 \Delta t \right) \quad (5.5)$$

which has units of dB relative to  $1 \mu\text{Pa}^2\text{s}$ .

These metrics were chosen to provide a broad characterization of the sound produced by pile driving and evaluate the validity of the computational model in providing an accurate representation of the noise. PSD evaluates the signal power at each frequency in the model. PSD agreement between the model and simulation is important due to frequency dependence in

species sensitivities. Also, agreement in levels and roll-off at multiple ranges indicate that the model is properly accounting for frequency dependent attenuation over long ranges. SPL is a characterized of the evolution of the impact waveform over time, and is important because certain time domain characteristics, such as the time from signal incidence to maximum amplitude, and also enter into species sensitivity considerations. Finally, the SEL is useful because it provides a single number characterization of the amount of energy present at any location and is particularly useful for assessing the total cumulative effects over time.

#### **5.4 POWER SPECTRAL DENSITY AND SOUND PRESSURE LEVEL COMPARISONS**

Power Spectral Density (PSD) is compared to acoustic data in Figure 5.6, Figure 5.7, Figure 5.8, and Figure 5.9, where each figure corresponds to a different pile. Comparisons show good agreement with both the FDTD and Empirical source models. While the empirical source model forces good agreement at the close range observation with the spectral weighting function, the FDTD source model by contrast has no such weighting. Beyond the close range comparisons, the continued favorable agreement in roll off show that the geoacoustic model is attenuating the waveforms accurately across the whole frequency band.

While some of the deviations between the model and acoustic data are caused by environmental simplifications inherent in the model, the main cause of disagreement is due to peaks and nulls. Peaks and nulls are produced by areas of constructive and destructive interference caused by multipath interactions, and occur at integer multiples of a wavelength. In the band where discrepancies primarily occur, between 500 to 2600 Hz, the wavelength varies from 3 to 0.57 meters, which is well within the uncertainty in the locations of the acoustic observations and bathymetry measurements.

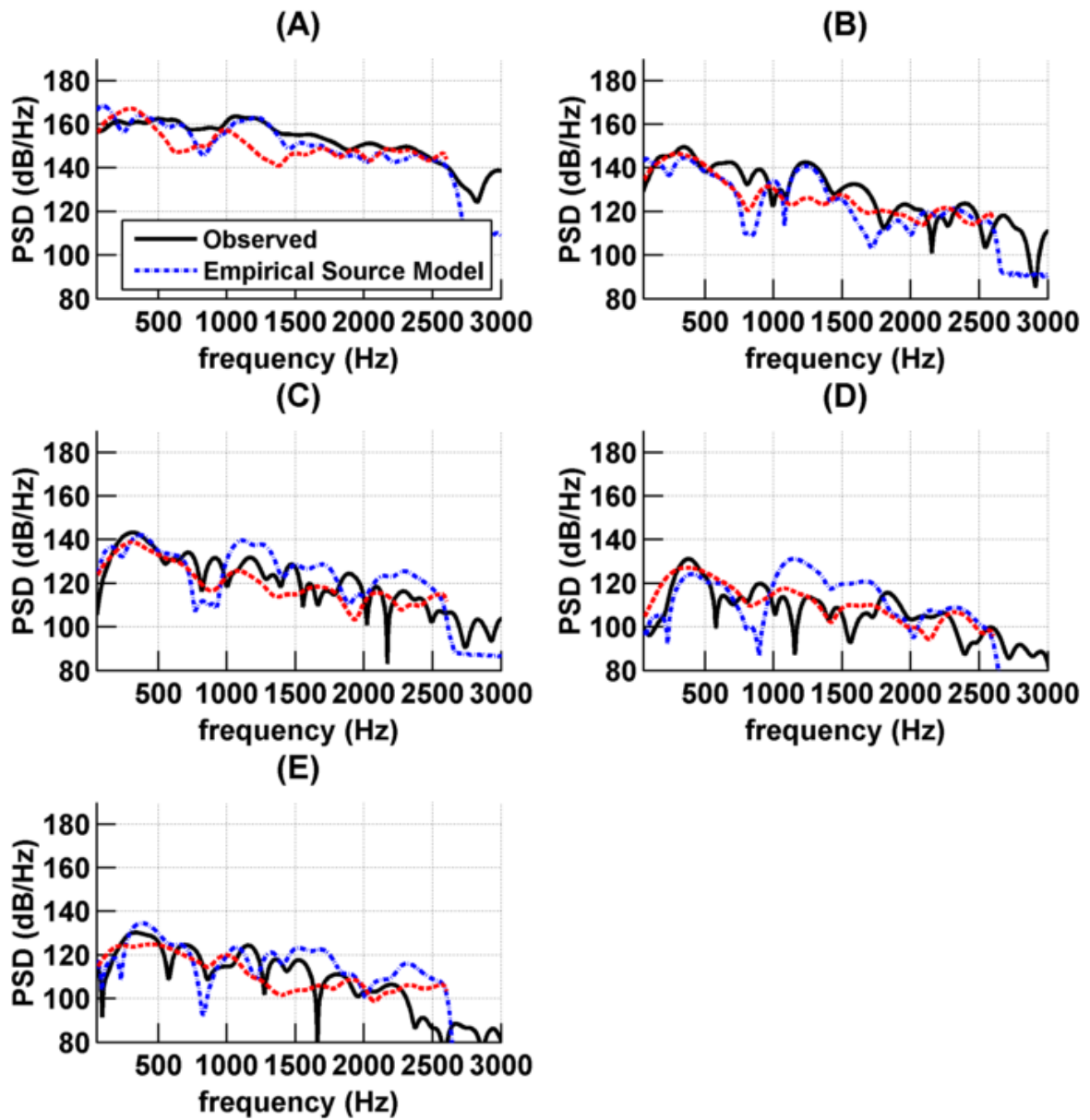


Figure 5.6: PSD comparisons for pile B1. Panel A corresponds to the 10m Observation site, B to 200m, C to 400m, D to 800m, and E to the 800m site in the opposite direction.

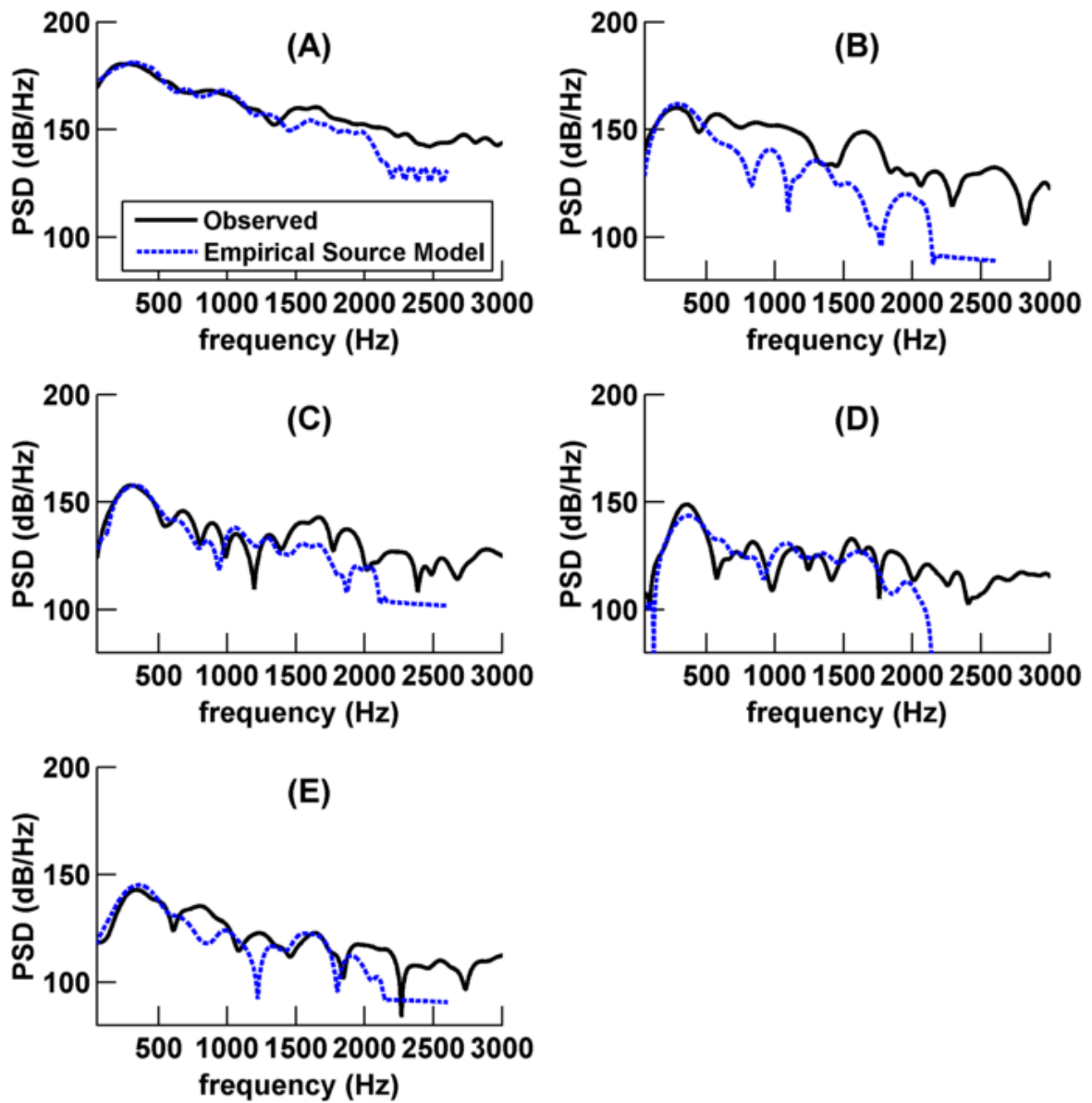


Figure 5.7: PSD comparisons for pile B2. Panel A corresponds to the 10m Observation site, B to 200m, C to 400m, D to 800m, and E to the 800m site in the opposite direction.

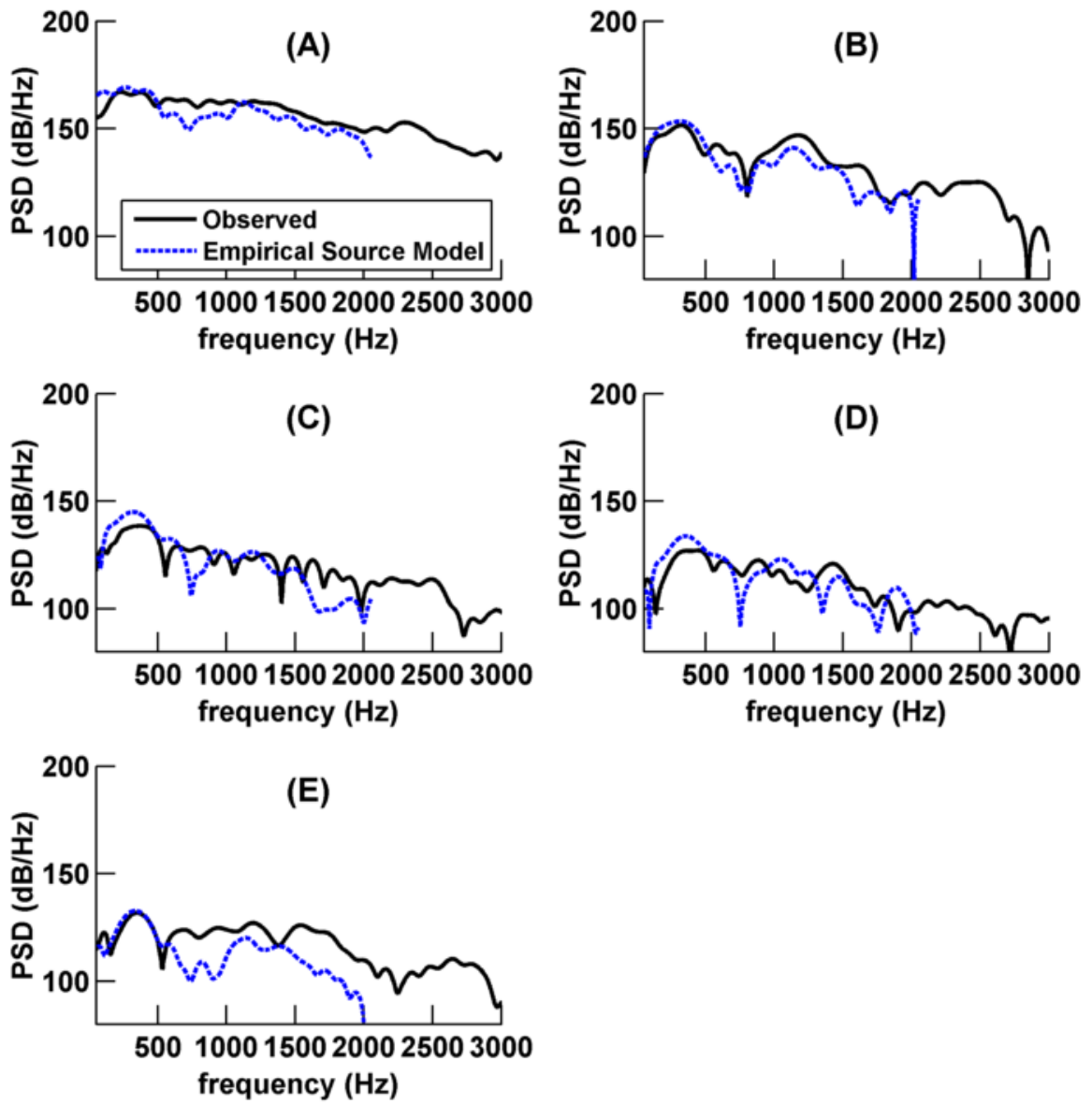


Figure 5.8: PSD comparisons for pile A1. Panel A corresponds to the 10m Observation site, B to 200m, C to 400m, D to 800m, and E to the 800m site in the opposite direction.

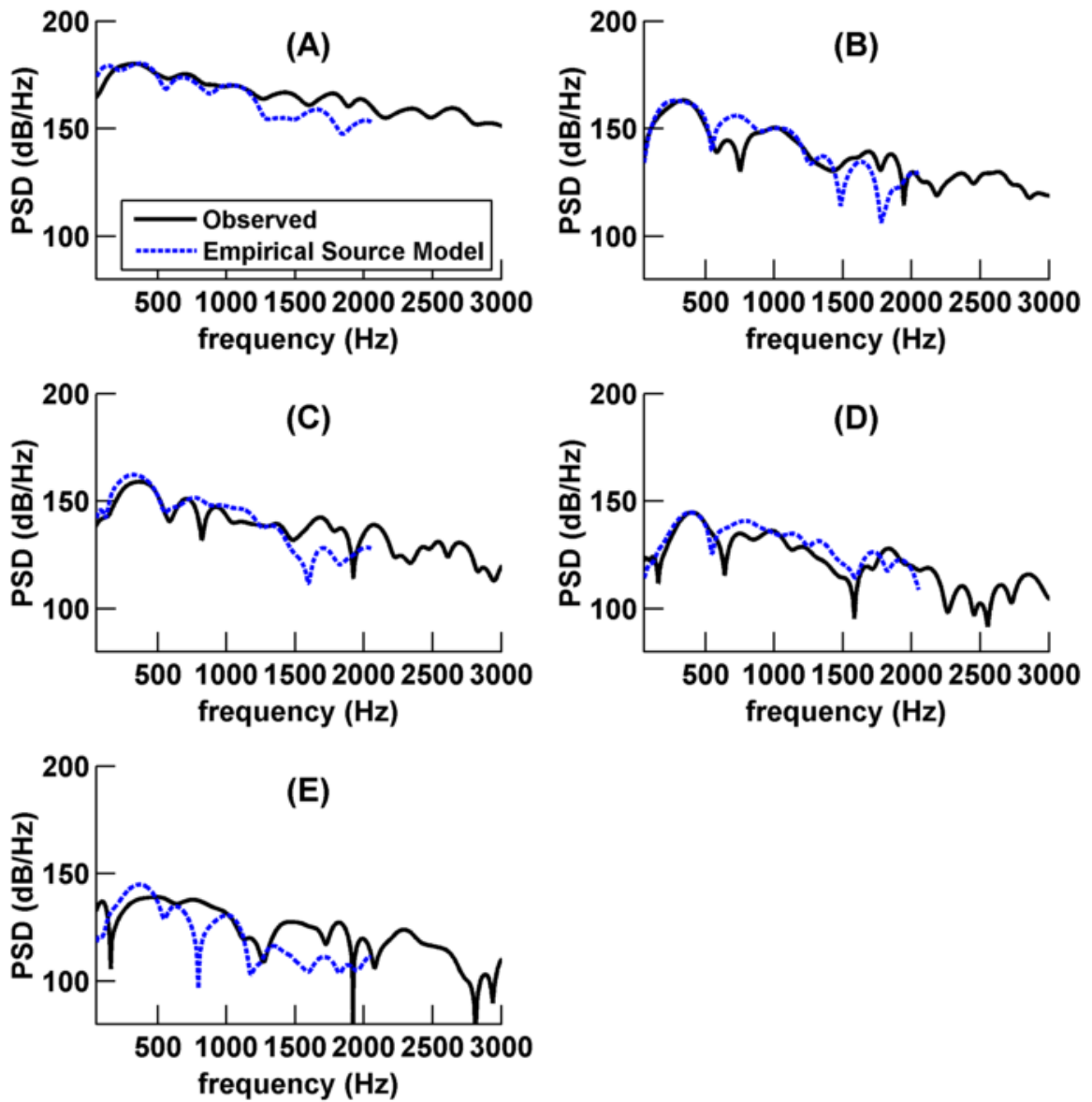


Figure 5.9: PSD comparisons for pile A3. Panel A corresponds to the 10m Observation site, B to 200m, C to 400m, D to 800m, and E to the 800m site in the opposite direction.

SPL comparisons also showed good agreement in the absolute levels, shown in Figure 5.10, Figure 5.11, Figure 5.12, Figure 5.13, and Figure 5.14. Matching specific peaks was intractable beyond very close range, due to uncertainty in measurement locations. The empirical source model showed the best agreement in matching the peaks, because the attenuation factor could be chosen to best match the close range waveform.

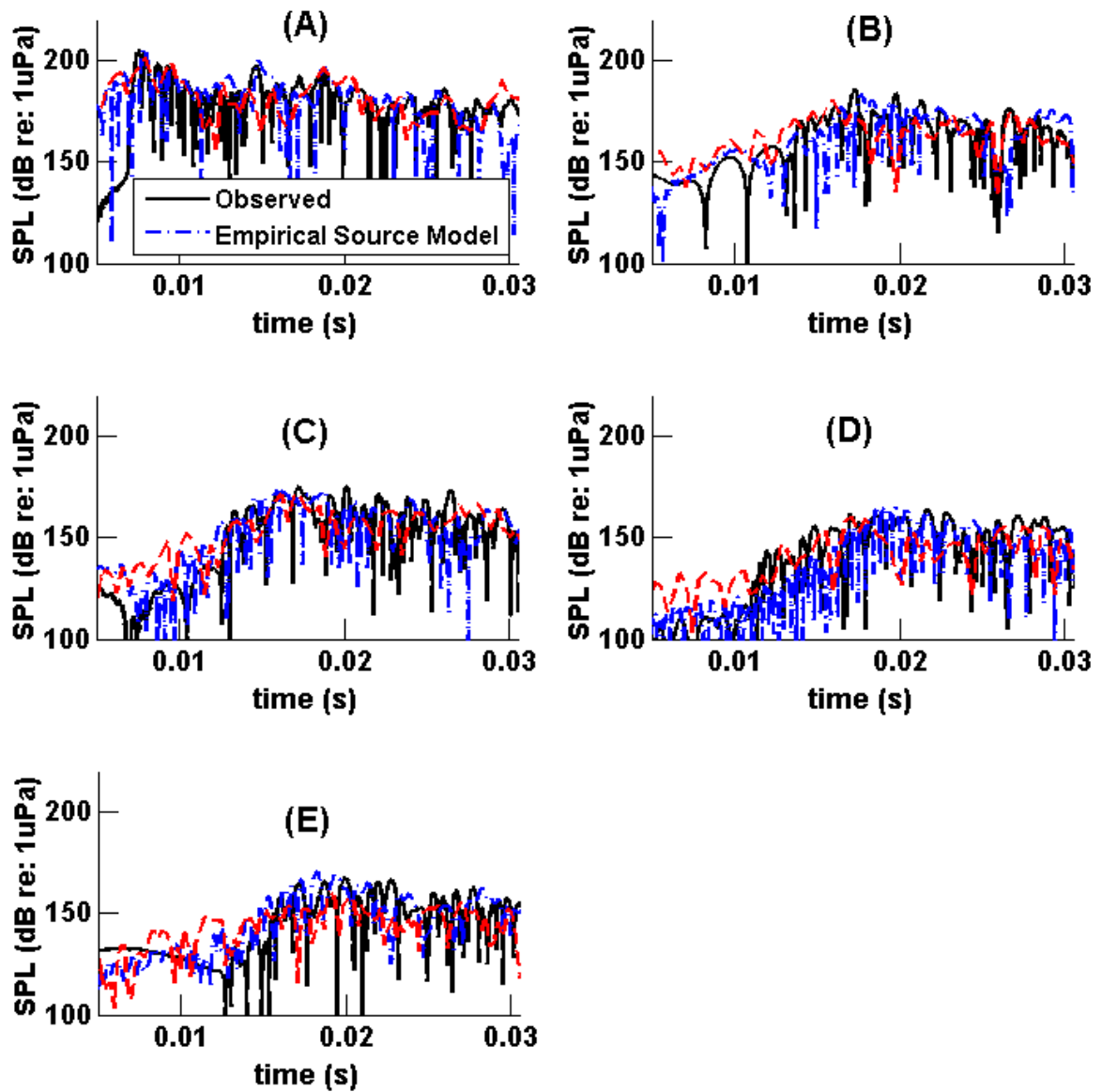


Figure 5.10: SPL comparisons for pile B1. Panel A corresponds to the 10m Observation site, B to 200m, C to 400m, D to 800m, and E to the 800m site in the opposite direction.

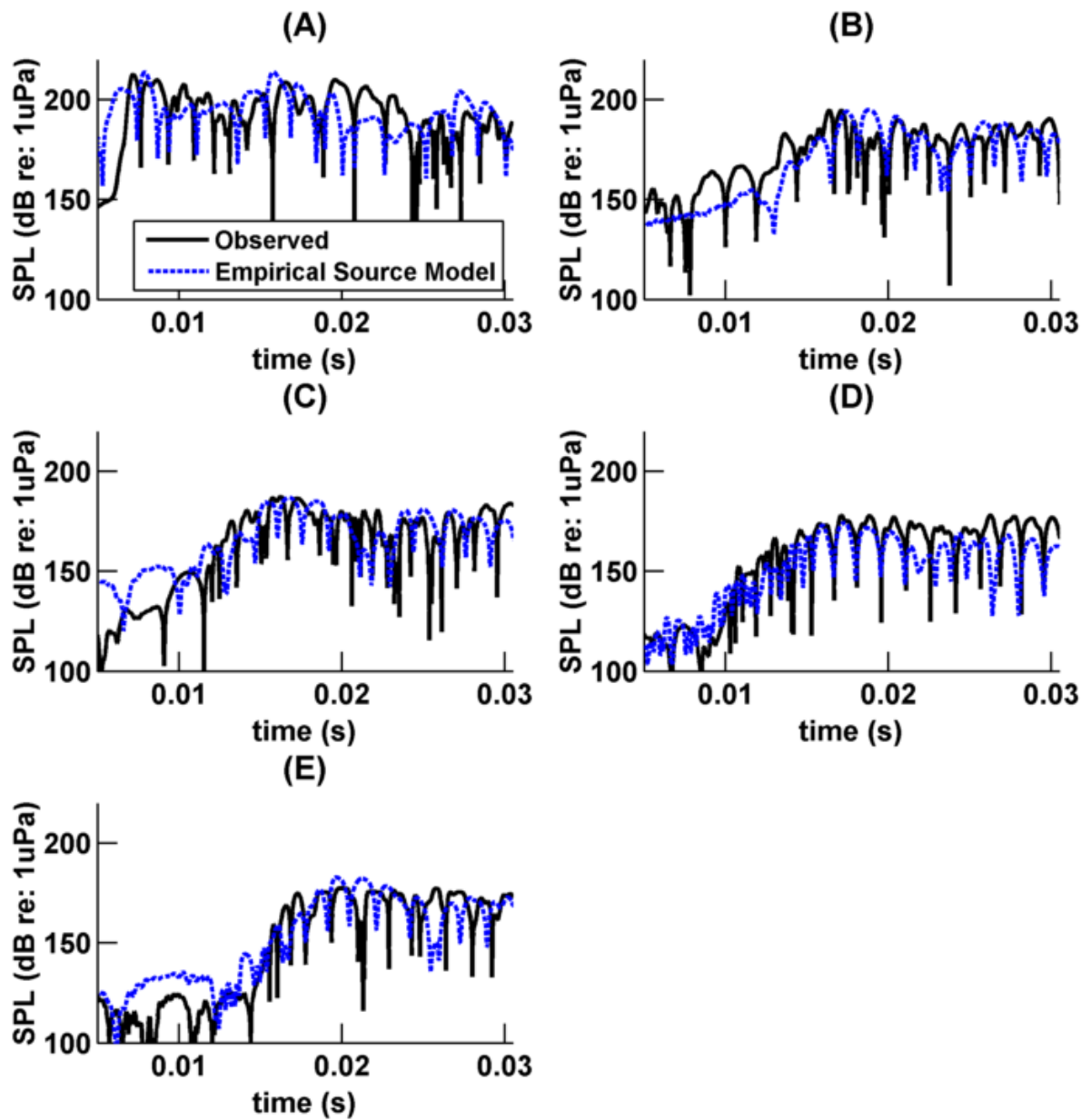


Figure 5.11: SPL comparisons for pile B2. Panel A corresponds to the 10m Observation site, B to 200m, C to 400m, D to 800m, and E to the 800m site in the opposite direction.

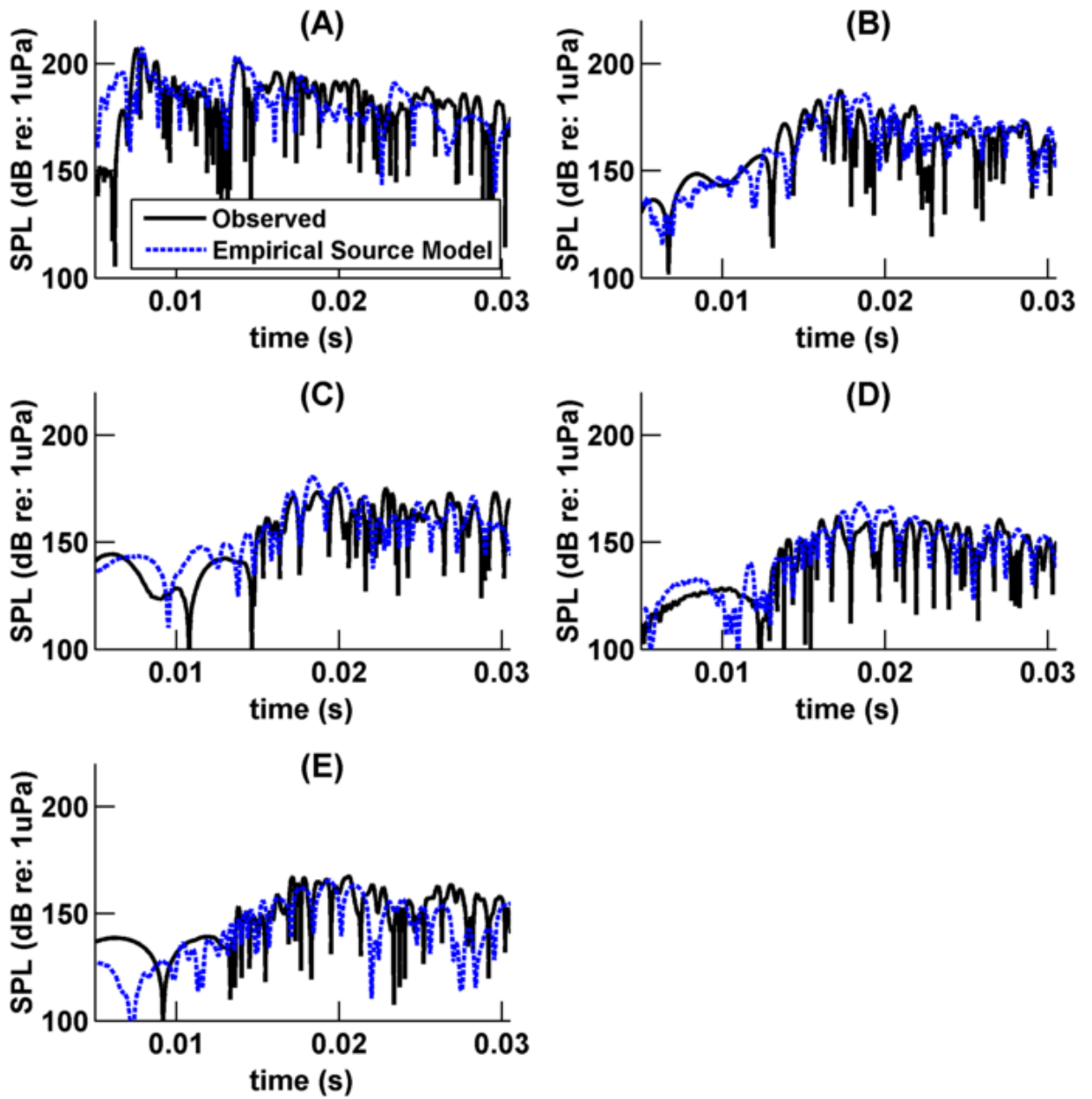


Figure 5.12: SPL comparisons for pile A1. Panel A corresponds to the 10m Observation site, B to 200m, C to 400m, D to 800m, and E to the 800m site in the opposite direction.

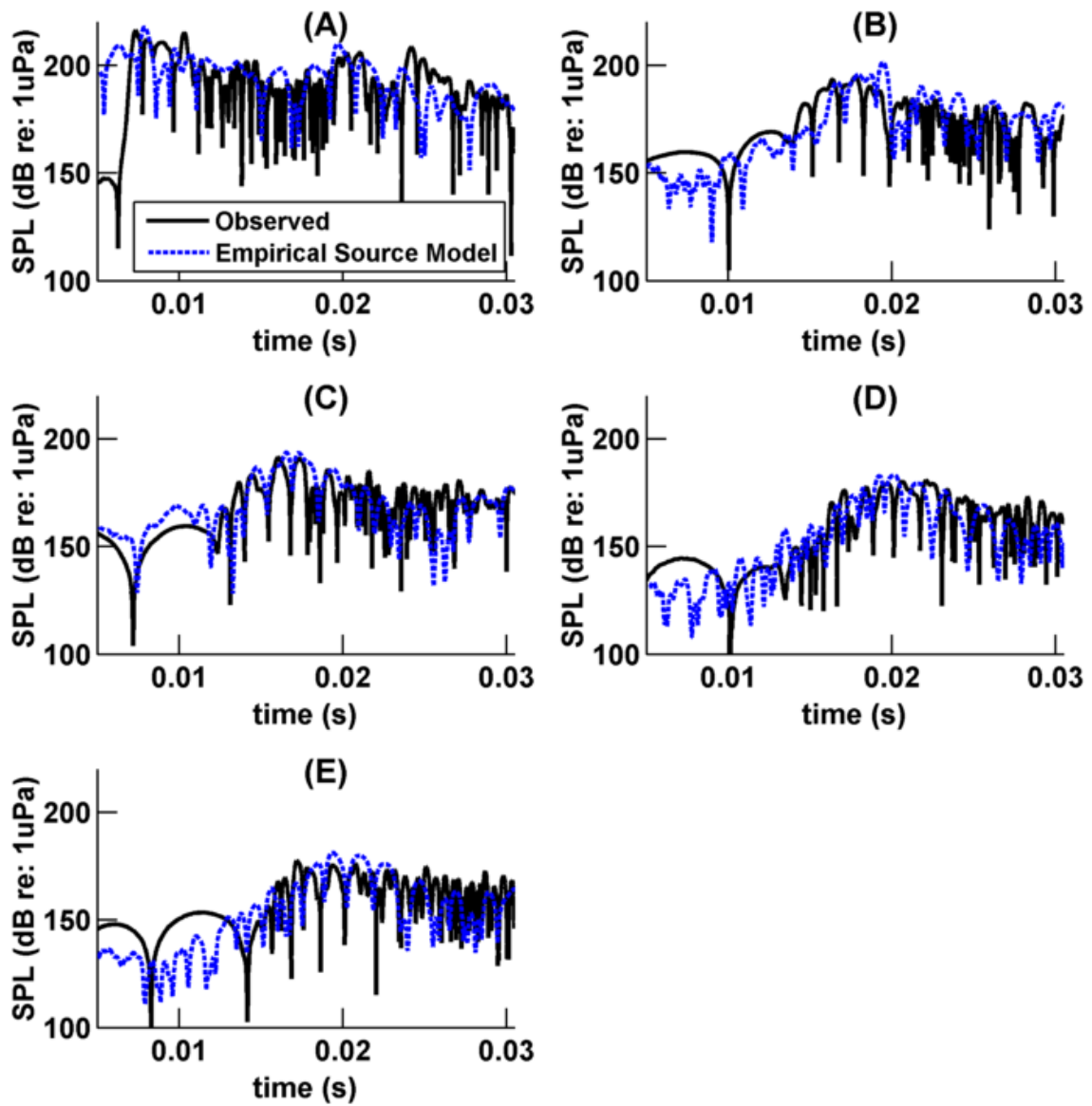


Figure 5.13: SPL comparisons for pile A3. Panel A corresponds to the 10m Observation site, B to 200m, C to 400m, D to 800m, and E to the 800m site in the opposite direction.

## 5.5 SOUND EXPOSURE LEVEL COMPARISONS

The SEL predicted by the model is compared to observations graphically in Figure 5.14. Table 5.2 numerically summarizes the cumulative SEL for each pile and observation site, as well as the deviations between the model and observations. The differences show the dB discrepancy between the model and observations, and the average of the difference is shown in the Average Pile Error column. The average difference at each measurement distance is shown in the Distance Average Error row. The average of all discrepancies is 2.17 dB.

The agreement is very encouraging. In 22 of 25 comparisons, the model agrees with observation to within 4 dB, where all instances of disagreement greater than 4dB occurred at the 800 meter observation locations. Also, all instances of large disagreement occurred at pile site B, where there is more variance and uncertainty in the sediment. At the closer observation locations, the agreement was much better, within 3 dB at all observation locations. This suggests a high level of reliability in predictions within 400 meters.

The discrepancies between the model and observations primarily occurred on the north riverside and with the use of the FDTD source model. This could likely be accounted for by the uncertainty in the geoacoustic configuration along the north riverside that is exacerbated by the much shallower Troutdale formation in that area. Furthermore, some of the discrepancy with the FDTD source model is due the lack of assurance of exact agreement at the source, and can be seen by the 1.26 dB discrepancy at the source, and subsequent slight over-prediction at all ranges. The FDTD source is likely not in a final state of analysis at GTech and needs to be evaluated over more pile configurations before its relative effectiveness can be conclusively assessed.

**Table 5.2: Sound Exposure Level Summary. All entries are in units of dB re: 1 $\mu$ Pa<sup>2</sup>s.**

<b>Observation Distance</b>	<b>10 m</b>	<b>200 m</b>	<b>400m</b>	<b>800 m</b>	<b>- 800 m</b>	<b>Average Pile Error</b>
B1 Empirical	173.33	155.29	147.85	136.84	140.71	
B1 FDTD	174.76	153.31	146.30	134.51	134.08	
B1 Observed	173.50	155.74	149.89	139.36	142.12	
Empirical Difference	0.17	0.44	1.34	2.52	1.41	1.18
FDTD Difference	1.26	2.44	2.89	4.84	8.04	3.90
B2 Empirical	185.97	168.43	161.27	148.17	156.60	
B2 Observed	185.99	168.25	162.58	156.21	155.85	
Empirical Difference	0.02	0.18	1.31	8.04	0.76	1.67
A1 Empirical	175.84	158.66	151.49	140.76	139.25	
A1 Observed	175.87	156.53	149.32	137.27	142.09	
Empirical Difference	0.03	2.13	2.17	3.49	2.84	0.96
A3 Empirical	186.72	169.61	165.45	155.33	154.24	
A3 Observed	186.80	166.53	162.90	154.87	153.27	
Empirical Difference	0.08	2.72	2.55	0.47	0.97	1.32
Distance Average Error	0.10	0.90	0.32	1.94	1.94	

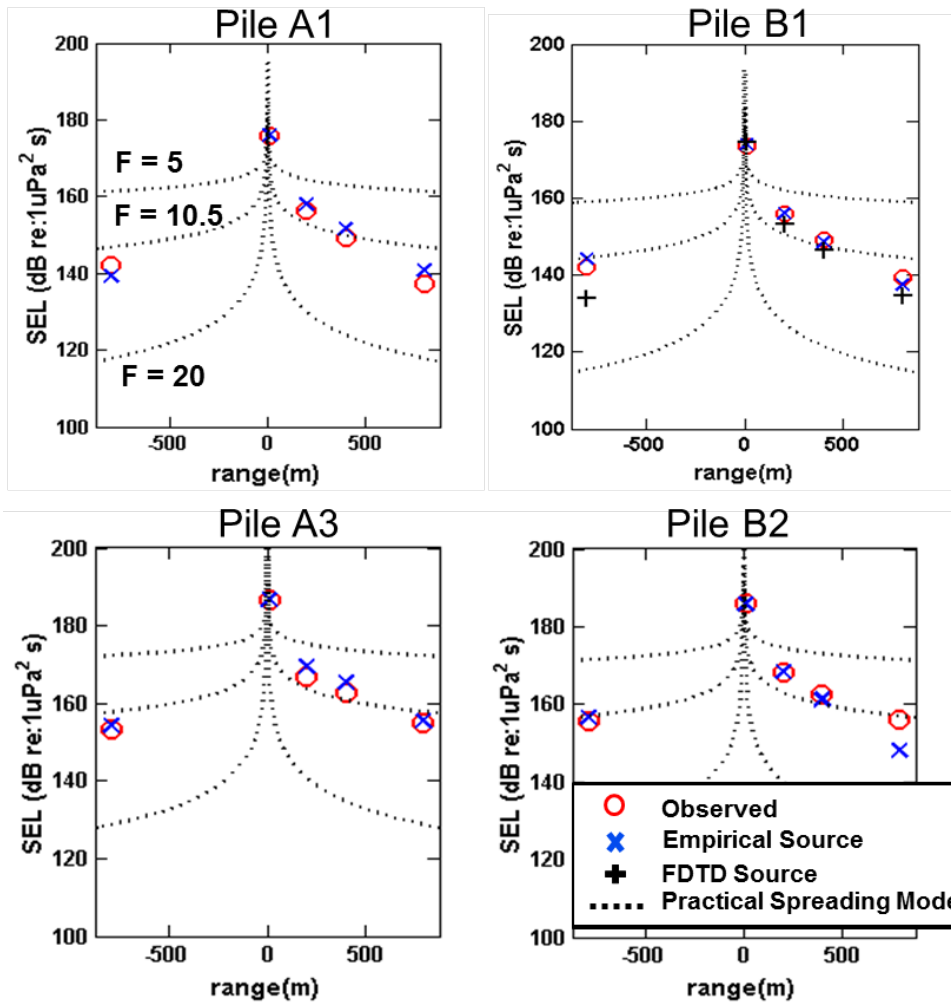


Figure 5.14: Sound exposure level summaries for each pile. The dotted lines correspond to results using the practical spreading model. The top line corresponds to an F factor of 5 and the bottom an F of 20. The middle line is a fit to the data, and corresponds to an F of 10.5.

Even with the slight discrepancies, the computational model can be seen to improve upon even the fit curve produced by the practical spreading model. It is worth noting that the fit curve ( $F = 10.5$ ) is based on the acoustic observations, which the computational model has improved upon with only a single acoustic measurement for the empirical source model and no measurements for the FDTD source model. Indeed, if the fit curve is assessed to be an adequate approximation of the sound levels, a practical application of the computational model could be to obtain F parameters, which could be used to generate quick and simple sound level predictions.

## **6.0 MODEL APPLICATIONS AND SITE CHARACTERIZATION**

The previous chapter established the validity of the source models and the propagation model by comparing results with measured data along multiple transects. Subsequently the model was extended to predict SEL over large portions of the Columbia River and characterize the effects of variable bathymetry and sediment configurations. Contour plots were generated from the solutions of several 2D simulations about a common source point. The effects of environmental configurations were quantified by comparing identical simulations, with only the parameter of interest varied. The simulations in this chapter demonstrate the relatively strong dependence of SEL on local environmental conditions and suggest that detailed environmental data is necessary to accurately predict areas where monitoring of pile driving activities is necessary.

### **6.1 CONTOUR PLOTS**

Contour plots were used to show sound level predictions in the Columbia River and demonstrate the improvement upon the predictions produced by the practical spreading model. These plots show the results of several simulations, run about a common origin point, and predict SEL produced by a pile-hammer impact. While the practical spreading model would simply produce concentric circles surrounding the pile driving site, significant variation from this can be seen in the contour plots. The sources of the irregularities are the inhomogeneities in the environment. That is, the variations in sediment depths and bathymetry, which are examined in greater detail below.

Contour plots are shown for piles B1 (Figure 6.1) and A3 (Figure 6.2). In general, the variation is greater on the north riverside, where the bedrock layer is much shallower and bathymetry variation is greater. One interesting section is to the northeast of the pile in Figure 6.1. While deeper water causes less attenuation over long range, this area produces a very sudden attenuation. This particular discrepancy is caused by the waveform experiencing spreading greater than cylindrical spreading in this region, due to the suddenly deeper water. The effect of these variations underscores the need for more advanced predictions of this nature, since the distance required for sound levels to fall below a given threshold can vary greatly depending on the bearing angle, which is not accounted by the practical spreading model.

## SEL Predictions About Pile B1

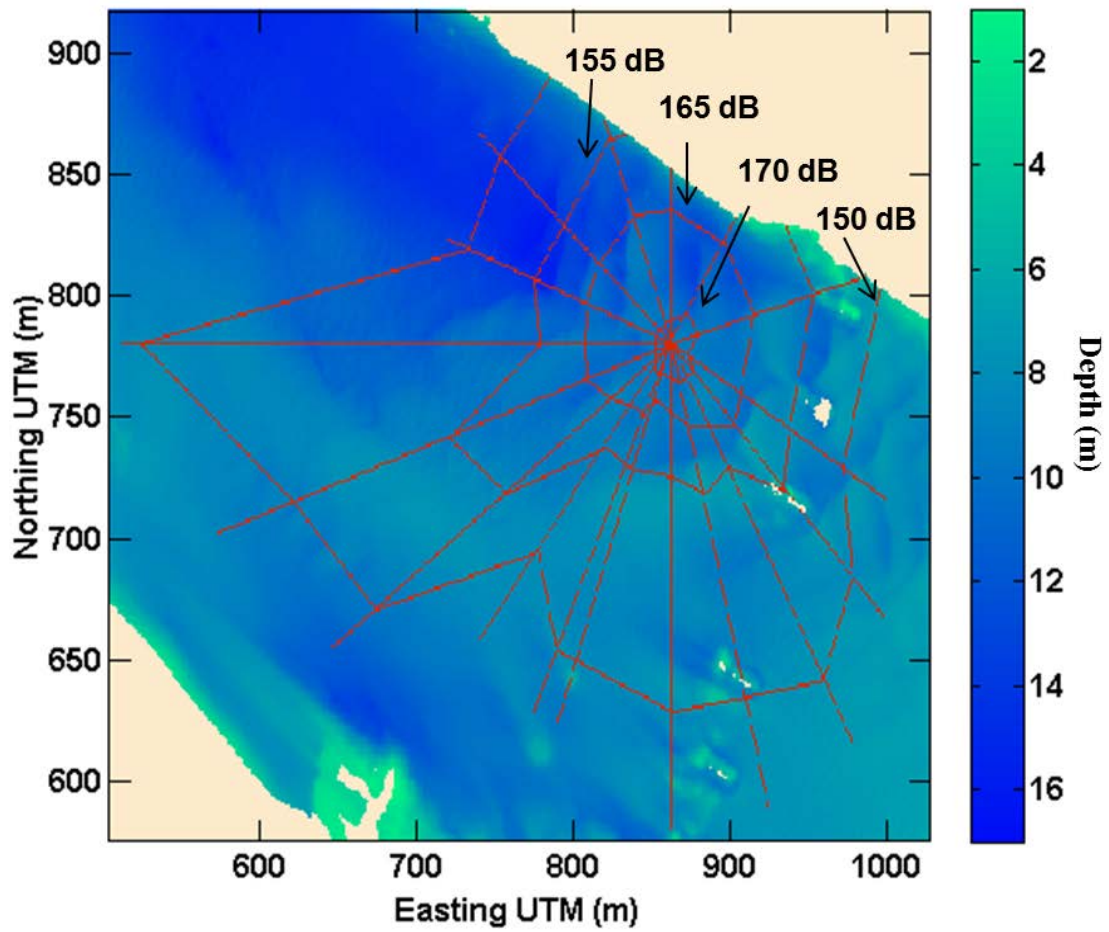


Figure 6.1: SEL contour plot about pile B1. The radial lines demarcate two-dimensional simulation results, and the lines connecting radials connect points of equivalent SEL.

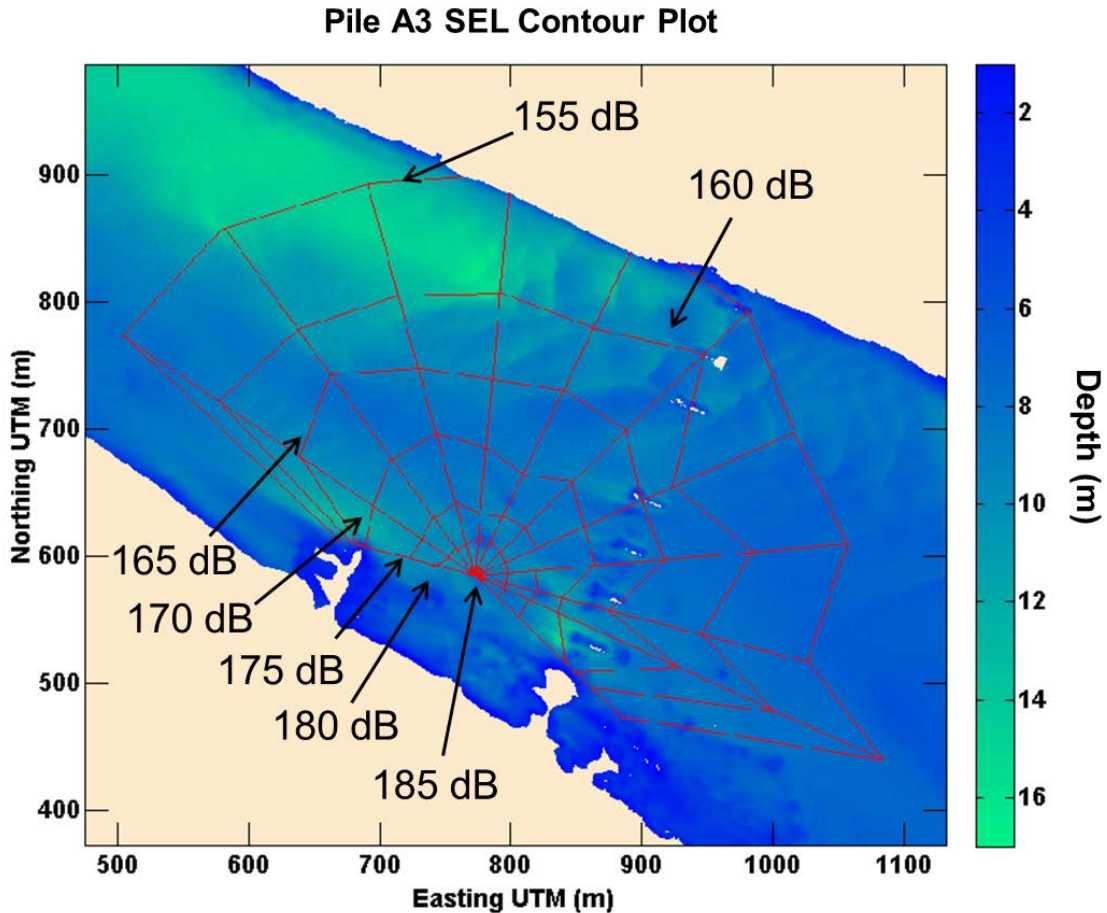


Figure 6.2: SEL contour plot about pile A3. The radial lines demarcate two-dimensional simulation results, and the lines connecting radials connect points of equivalent SEL.

## 6.2 CHARACTERIZATION OF BATHYMETRY VARIATIONS

The effect of bathymetry on SEL was studied by selecting several characteristic test cases from the Columbia River bathymetry. The test cases shown in Figure 6.3 were sections of bathymetry that encompassed the extremes of bathymetry variation in the neighborhood of pile driving operations. The effect of variations in bathymetry was quantified by calculating otherwise identical simulations, with the different pieces of bathymetry from the Columbia River used. Pieces of bathymetry were chosen to include as many of the features present in the environment as possible.

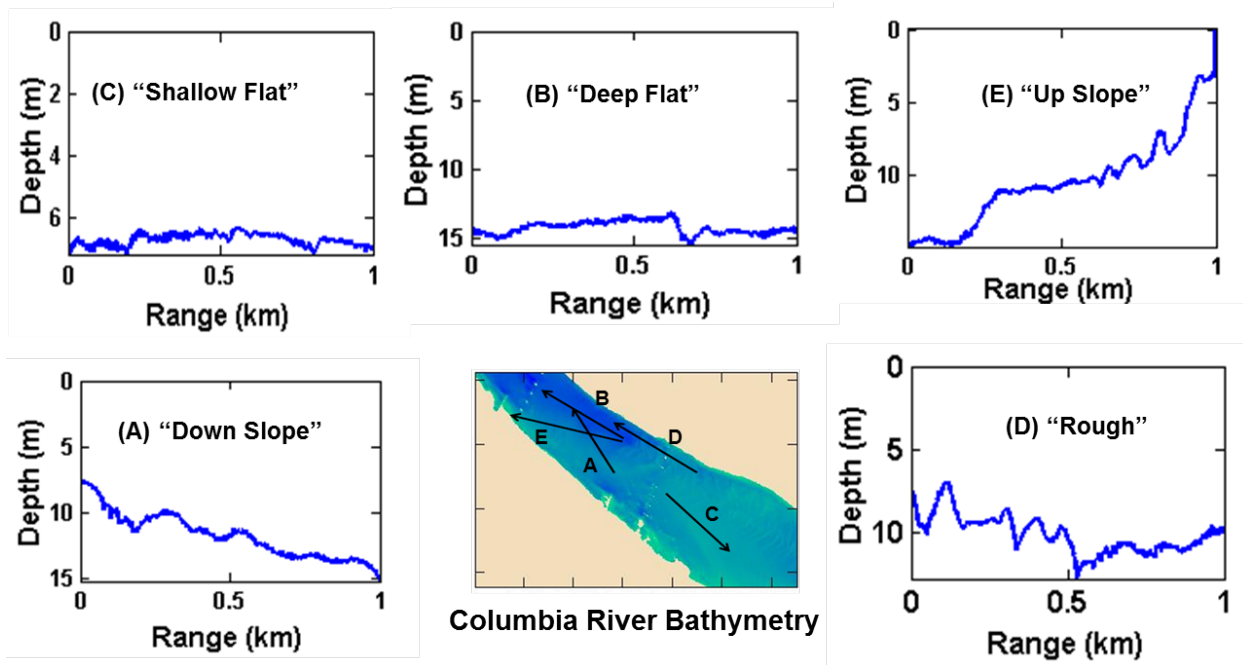


Figure 6.3: Five bathymetry test cases, located near the I-5 Columbia River crossing. Test cases encompass the deep and shallow extremes, as well as the extremes for roughness and sloping bottoms found in the neighborhood of the construction site. Test cases are taken from the Bathymetry at center and correspond to the labeled arrows.

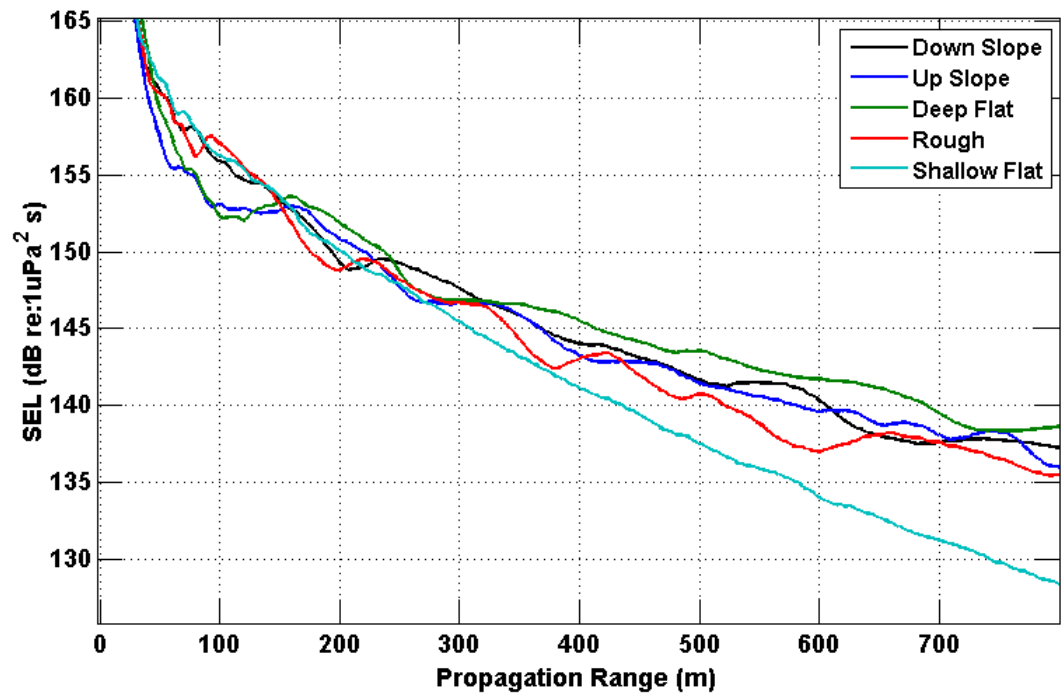


Figure 6.4: Range dependent SEL at a depth of 3.5m, for each bathymetry test case.

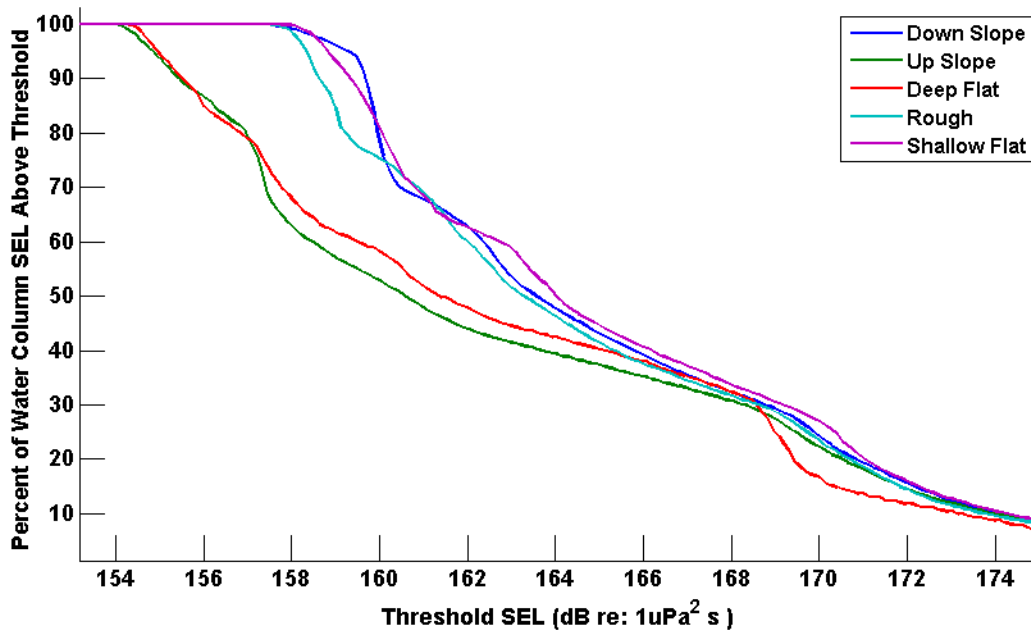


Figure 6.5: Statistical threshold plot comparing the percent of the water column SEL above certain thresholds, for the different test cases. The region of comparison comprises the water column from range 100m to 200m.

Figure 6.4 shows the range-dependent SEL for the analysis of bathymetry and sediment effects. For most of the variable bathymetry test cases there are only local variations of less than 5 dB, and only the average water depth over long distances significantly affects sound levels, due to increased sediment interactions over long range. Examining the SEL curve corresponding to the rough bathymetry, deeper sections produce lower sound levels as the sound freely expands into a greater area, but sound levels increase in the shallower regions as the signal energy is concentrated into a smaller area. Figure 6.5 depicts how the SEL varies with depth by plotting the percent of the entire water column that is above a range of SEL values at a distance of from 100m to 200m from the source. The “Rough” and “Deep Flat” profiles have noticeably larger portions of the water column with SEL values in the range of 155 to 164 dB.

### 6.3 CHARACTERIZATION OF SEDIMENT CONFIGURATIONS

The model was also applied to quantify the effects of various sediment configurations. The sediment configurations of interest are the position of the dense, highly reflective Troutdale formation and the composition of the top layer. The effect of the Troutdale formation depth was studied by computing solutions with variable bedrock depths that were otherwise equivalent. Figure 6.6 and Figure 6.7 show the results of the bedrock layer comparisons. Variations in the shallow water bedrock has the greatest effect, while bedrock layers of depths greater than 25 meters have little practical effect on the SELs present in the water column for the medium sand top layer of the Columbia River. The 15.5 meter bedrock depth curve shown corresponds to the layer depth used in the comparisons to acoustic data.

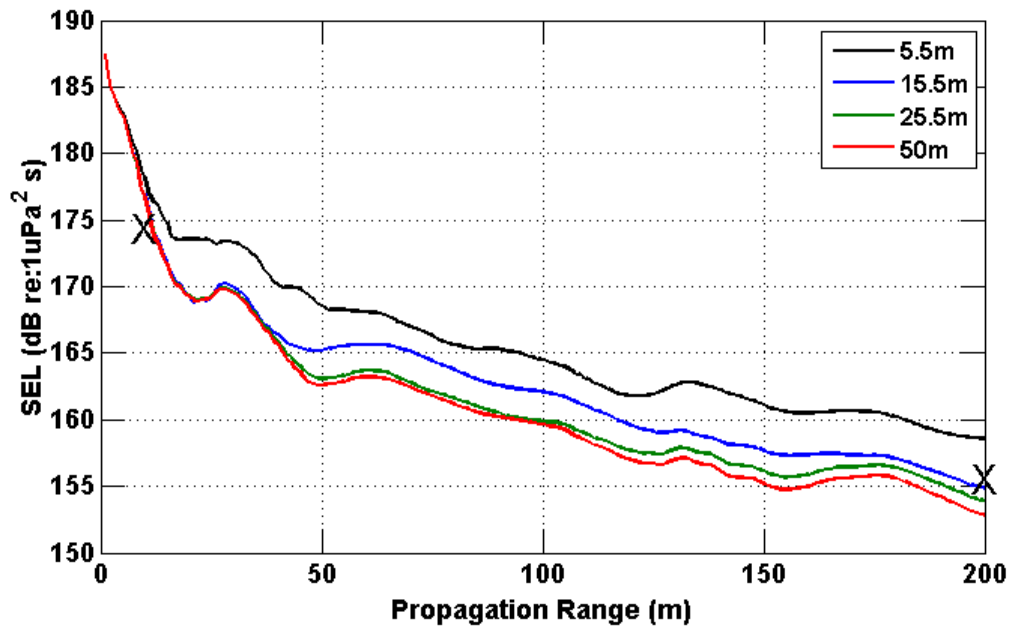


Figure 6.6: Range dependent SEL at 3.5 meter depth for multiple bedrock depths about pile B1. X demarcates the acoustic observations. Bedrock depths are relative to the simulation bathymetry.

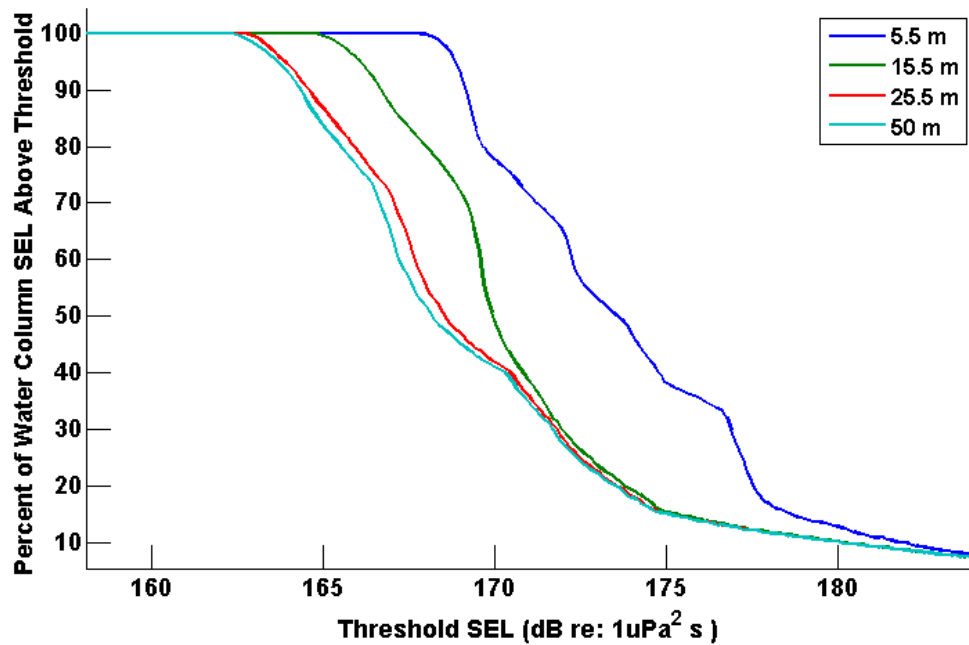


Figure 6.7: Statistical threshold plot comparing the percentage of the water column above certain SELs, for several bedrock depths. Again, variations in a shallow bedrock layer have the greatest effect, and bedrocks below 25 meter depth have little practical effect on the water column SEL. The region of consideration is the water column from range 100 to 200 meters.

The effect of the top layer is analyzed by comparing simulated results using various published parameters, describing alternate sediment compositions. The parameters used for comparison of the top sediment layer are summarized in Table 6.1. Sediments with large sand portions were emphasized to examine the effects of mixing the sandy bottom of the Columbia River with additional soil components. All parameters are standard values from the literature (*APL-UW 1994*).

**Table 6.1: Parameters for Top Sediment Layer Comparison**

	<b>Attenuation (dB/λ)</b>	<b>Density (g/cc)</b>	<b>Sound Speed (m/s)</b>
Sandy Clay	0.0890	1.147	1420
Sandy Mud	0.2107	1.490	1420
Sandy Gravel	0.9306	2.492	1936
Coarse Silt	1.177	1.195	1472

The result of the top layer comparison is shown in Figure 6.8 and Figure 6.9. In general, the curves show a complex relationship between density and attenuation on SEL, with neither sound speed nor density having a dominant effect. The Sediment layer curves are similarly shaped for each sediment configuration except sandy clay, where there is a dramatic spike in SEL at about 370 meters. In the case of sandy clay, the signal is attenuated very little in the sediment, and the large spike peaking at 370 meter range corresponds to the reflection of the first arrival off from the Troutdale formation, which is at a depth of 51.5 meters for pile A3. This is diagramed in Figure 6.10, where the reflection of the first arrival from the bedrock layer can be seen to reach the receiver at approximately 371 meters. This is an important result, because it predicts that dramatic SEL spikes are possible at long range for environments that include low attenuation and density top layers, coupled with dense bedrock layers, even if those bedrock layers are very deep.

Furthermore, recalling the practical spreading model solutions in Figure 3.3, most of the sediment configurations appear that they could be reasonably approximated using the practical spreading model. A potential application of this method could be to determine the F parameter for a configuration of interest, or as in the case of Sandy Clay, determine where the simplified predictions are not sufficient.

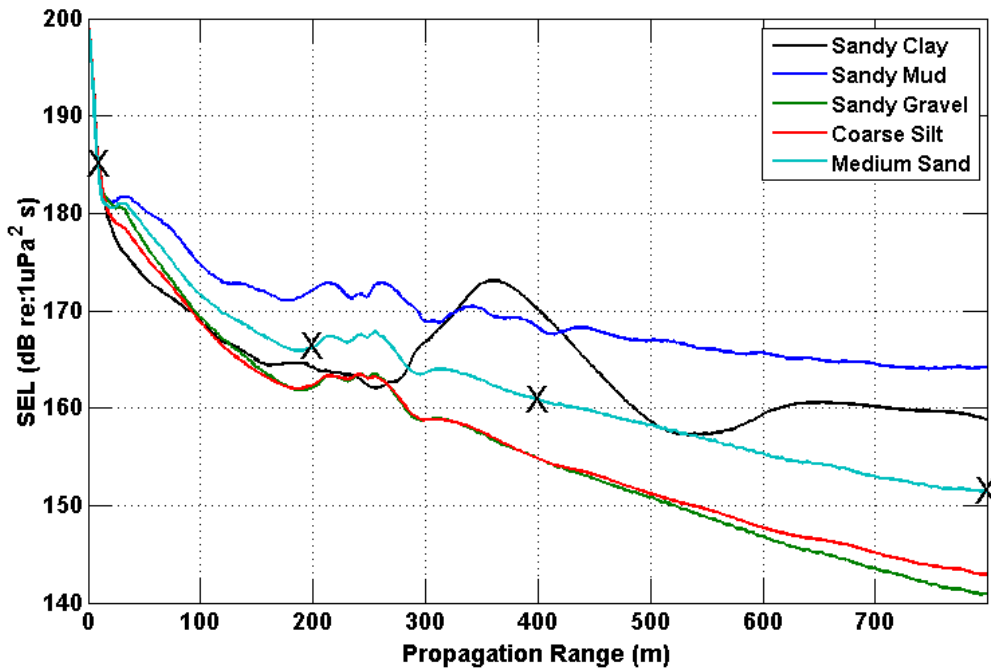


Figure 6.8: Range dependent SEL at 3.5m depth, for the top layer compositions in Table 6.1, about pile A3. X marks the observed SEL.

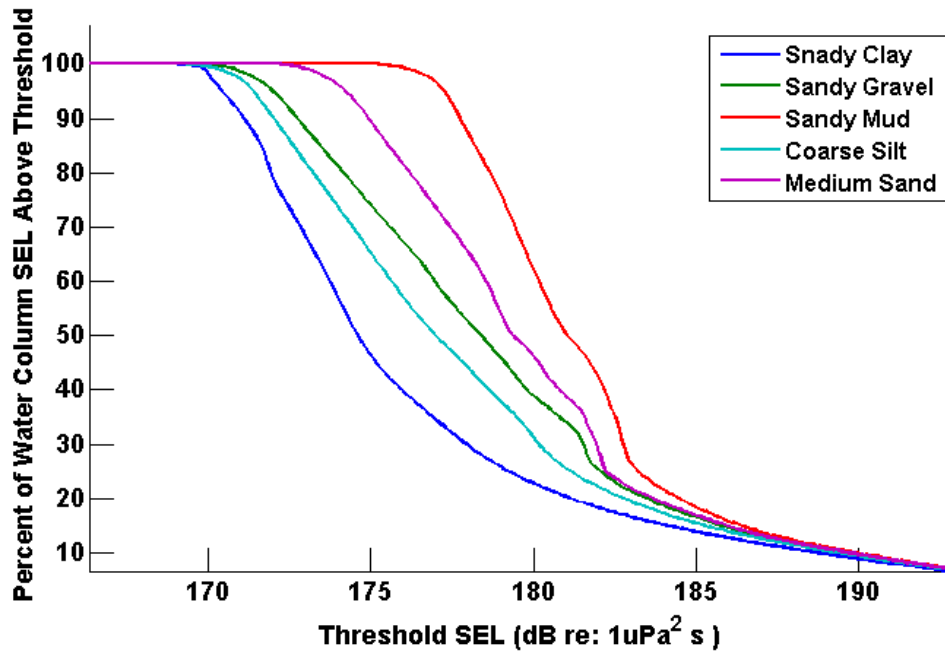


Figure 6.9: Statistical threshold plot comparing the percentage of the water column about certain SEL, for each top layer composition. The area of interest is the water column from range 100 to 200 meters.

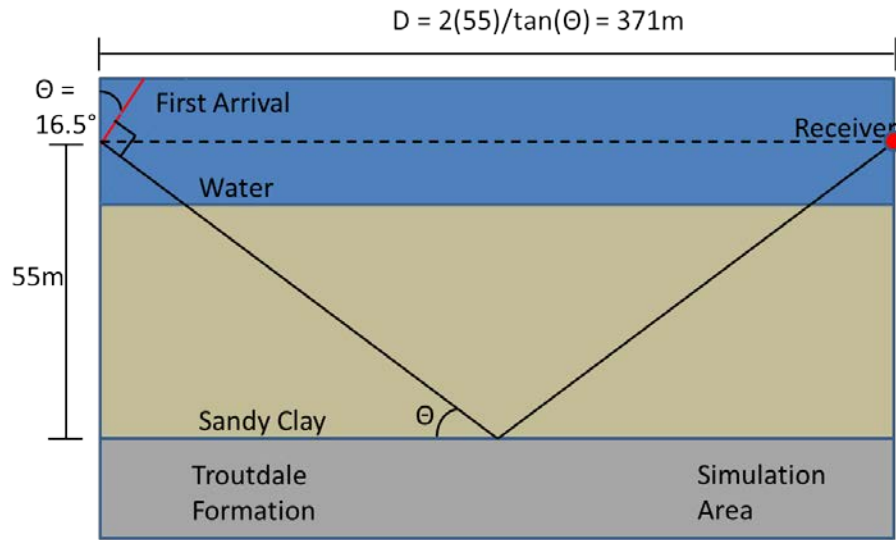


Figure 6.10: Geometrical explanation for the large SEL spike seen around 370 m in Figure 6.8. The propagation angle is assumed to change very little in the sediment due to the similar sound speeds.



## 7.0 CONCLUSION

Underwater impact pile driving is the source of increasing environmental and regulatory concern due the extremely high underwater sound levels radiated into the surrounding environment, which are known to harm marine wildlife. In this report the noise from underwater impact pile driving was analyzed with a computational model that used physical models of the pile driving source, coupled to a broadband synthesis of the RAM-PE, a PE based wave propagation tool. Source models included an empirical model from Reinhall and Dahl (2011) and an FDTD model from Shahab and Hastings (2011). These source models were coupled with convergent results produced by the RAM-PE that used a sediment model and bathymetry that are range-dependent.

The computational model was applied to the Columbia River environment between Portland, OR and Vancouver, WA, which was advantageous due to the environmental monitoring and site characterization done in preparation for the construction of the new I5 span. Environmental monitoring included acoustic observations of test pile observations in the North and South riversides performed by the consulting firm David Evans and Associates. Acoustic waveforms due to pile driving of 24 and 48 inch piles were recorded at 5 locations each, at ranges from 10 to 800m, which provided close and long range comparisons between the model and observation, providing 20 comparisons.

The model showed strong agreement with observations in PSD, SPL, and SEL. PSD comparisons show levels and roll off that are typically in very good agreement. Most of the features in the observed data are captured in SPL comparisons at close range, and at longer propagation ranges, the levels are accurately predicted. SEL agrees within 4 dB at all but 3 of 25 comparisons, and usually the agreement is much better, to within 2dB. Within 400m range, SEL shows very good agreement at all observation locations.

Beyond comparisons to acoustic data, the model was applied to produce SEL contour plots over large areas of the Columbia River environment and study the effects of bathymetry and sediment configurations. The absolute depth of the bathymetry is found to be the only factor that significantly affects long-range sound levels, while other variations create only localized effects. Also, the bedrock layer is determined to be insignificant when deeper than 25m below the mud line for the medium sand layer present in this region of the Columbia River.

The modeling presented in this work showed significant improvement over current sound prediction techniques, specifically the practical spreading model, with less reliance upon acoustic data. While the final application of this modeling work may be to determine practical spreading model parameters reliably and efficiently, the analysis in Section 6 showed that certain environments produce sound characteristics that the practical spreading is not sufficient to account for under any choice of parameters. In those cases it is necessary to use modeling techniques such as those presented here to fully account for the sound characteristics.

While the model showed strong agreement in the Columbia River environment near the new Columbia River Crossing, it has not been tested in other environments. Future work should apply the model to environments with bathymetry and sediment composition differing from the

environment presented in this thesis. Furthermore the present modeling does not take into account the attenuation effects of shear waves, and should be included. Also, the FDTD analysis used was preliminary and needs further analysis and development.

## 8.0 REFERENCES

- APL-UW. *High-Frequency Ocean Environmental Acoustic Models Handbook*. Applied Physics Laboratory. University of Washington. 1994.
- Collins, M.D. A Split-step Padé Solution for the Parabolic Equation Method. *Journal of the Acoustical Society of America*, Vol. 93, 1993, p.1736-1742.
- Columbia River Crossing (CRC). *CRC Geotech Reports: Appendix B Boring Logs*. February, 2011a
- Columbia River Crossing (CRC). *CRC Geotech Reports: Appendix F Laboratory*. February, 2011b
- Edmondson, A.J. Solution of Shell Problems by the Finite Difference Method. *Nuclear Engineering Design*. Vol. 11, No. 2, 1970, p. 208-216.
- Goldberg, J.E., and T. Korman. A Finite Difference Formulation of General Shell Equations. *Nuclear Engineering Design*. Vol. 26, No. 3, 1974, p. 440-443.
- Hamilton, E.L. Geoacoustic Modeling of the Sea Floor. *Journal of the Acoustical Society of America*. Vol. 68, No. 5, 1980, p. 1313-1340.
- Hardyniec, S., and S. Skeen. Pile Driving and Barotrauma Effects. *Journal of the Transportation Research Board*. Vol. 1941, 2005, p. 184-190.
- Hastings, M.C., and A.N. Popper. *Effects of Sound on Fish*. California Department of Transportation Contract No. 43A0139. 2005.
- ICF Jones and Stokes. *Technical Guidance for Assessment and Mitigation of the Hydroacoustic Effects of Pile Driving on Fish*. California Department of Transportation. 2009.
- Ifeachor, E.C., and B.W. Jervis. *Digital Signal Processing: A Practical Approach*. Addison-Wesley, NY. 1993.
- Jensen, F.B., W. A. Kuperman, M.B. Porter, and H. Schmidt. *Computational Ocean Acoustics*. AIP Press/Springer, New York. 1994.
- Junger, M.C. Acoustic Fluid-Elastic Structure Interactions: Basic Concepts. *Computers and Structures*. Vol. 65, Issue 3, 1997, p. 287-293.
- Kinsler, L.E., A.R. Frey, A.B. Coppens, and J.V. Sanders. *Fundamentals of Acoustics*. Wiley, New York. 2000.

Reinhall, P.G. and P.H. Dahl. Underwater Mach Wave Radiation from Impact Pile Driving: Theory and Observation. *Journal of the Acoustical Society of America*. Vol. 130, No. 3, 2011, 1209-1216.

Shahab, S., and M.C. Hastings. Transient Analysis of Sound Radiated from a Partially Submerged Cylindrical Pile under Impact. *Journal of the Acoustical Society of America*. Vol. 132, No. 3, 2011, p. 2034.

Stockham, M.L., P.G. Reinhall, and P.H. Dahl. Characterizing Underwater Noise from Industrial Pile Driving at Close Range. Proceedings of IEEE Oceans, 978-1-4244-4332-1, 2010.

Stokes, A., K. Cockrell, J. Wilson, D. Davis, and D. Warwick. *Mitigation of Underwater Pile Driving Noise During Offshore Construction*. Final Report. Department of the Interior, Minerals Management Service, Contract Number: M09PC00019. 2010.

Warburton, G.B., "Vibration of a cylindrical shell in an acoustic medium," Proc. Inst. of Mech. Eng. Part C-J. Eng. Mech. Eng. Sci. 3, 69-79 (1961).

Würsig, B., C.R. Greene, and T.A. Jefferson. Development of an Air Bubble Curtain to Reduce Underwater Noise of Percussive Piling. *Marine Environmental Research*, Vol. 49, 2000, p.79-93.

## **APPENDIX A - MODEL IMPLEMENTATION**



This appendix discusses the details of the computational model implementation, and should be a sufficient first reference for further modeling work. The computational pile driving model uses a primary propagation code for both source models. Additionally, depending on the source model, pre-processing and post-processing routines are used. For both source models, the result is a 3 dimensional matrix of depth, range and frequency, which defines the broadband propagation over a 2 dimensional slice of environment. Single or multiple 2D solutions were processed to produce graphical and quantitative results, in the time and frequency domain, for comparisons with data and prediction of sound levels. All modeling was implemented in the MATLAB language.

## **8.1 FDTD SOURCE PRE-PROCESSING**

The FDTD pre-processing routine calculated the initial pressure solutions, defined by equation (4.13), for convolution with the RAM-PE Green's functions. First, the time domain particle velocity solution was read in from the Excel spread sheet, provided by GTech. For each node, the time domain solution was zero padded to accommodate the user specified frequency resolution (to correspond to the required broadband frequency resolution), transformed to the frequency domain via the DFT, and multiplied by the depth dependent specific acoustic impedance (4.11) as well as the other scaling factors in the expression for the starting fields (4.13). The pressure spectrum at each node is truncated to the user entered bandwidth requirements and windowed using a slight Tukey window (window factor of 0.015) to reduce ringing in the time domain synthesis. Finally, the result is saved along with the frequency and depth axis into a file to be called by the propagation code.

## **8.2 BROADBAND PROPAGATION MODEL**

Broadband propagation was handled using the publicly available code titled the RAM-PE (*Collins et al. 1996*). The RAM-PE is a FORTRAN code, and when executed draws the model parameters from an input script, which varied slightly depending on the source model. The parameters defined by the script were grouped into simulation, transect and environment parameters. Simulation parameters included the solution destination folder, the solution file name, and the range and depth span to be saved in the final solution. For the empirical source model, the number of arrivals modeled, depths of the point source solutions and bandwidth parameters were also defined. The FDTD source required that the source data file name be specified as well as which source depths were calculated. Since the contributions from source depths combine linearly, modeling only certain sources was useful for breaking up simulations over multiple computers. Transect parameters defined the source location, simulation bearing angle, and simulation length.

The environment parameters specified the geoacoustic model. The sediment depths (m), densities (g/cc), sound speeds (ms) and attenuation (dB/ $\lambda$ ) were specified in matrices, where each row defined the parameter for the sediment layer corresponding to the layer at the depth defined in the sediment spacing matrix. The model allowed an arbitrary number of range dependent updates in the geoacoustic model, which corresponded to the columns in the environmental parameter matrices. The ranges of these updates were specified in the update range matrix, where parameters were linearly interpolated between updates. Finally, the wetted pile length, total pile length and pile sound speed were specified for the empirical model.

The model first extracted the bathymetry using the source location, bearing angle and length from the Columbia River bathymetry data. The bathymetry simulation and environment data were then passed to the main propagation routine, which calculated the broadband propagation. This code executed RAM-PE for each of the frequencies, source depths and arrivals defined in the input file. For the empirical source model, it was only necessary to calculate the first two arrivals. Since RAMPE is a FORTRAN code, it was compiled as an executable (which required certain cygwin .dlls to be present) that was called using a system command in the MATLAB code. The input to RAM-PE is handled with a text file, which was written for each RAM-PE execution by the MATLAB code. RAM-PE also outputs a text file, which is read in by the MATLAB code and arranged into a matrix of depth of range. Since RAM-PE does not include the phase change associated with the movement of the wave front, a range dependent phase shift was applied to the solution. Finally, the result was truncated in range and depth to the user specified bounds, and placed in the three dimensional output matrix. This matrix was saved with the depth, range and frequency axis, as well as the bathymetry and sediment spacing information. The empirical source model saved each arrival in separate files.

### **8.3 EMPIRICAL SOURCE POST-PROCESSING**

For the empirical source, the propagation code alone calculated the phased Greens functions, summed over all source depths, for the first two arrivals, without offsets or spectral weighting. That is, the first two arrivals produced by the ringing bulge, of flat spectrum and equal, unit amplitude. The empirical post processing routine used these pieces to assemble to final simulation. The user entered parameters included the file names of the arrivals, the attenuation factor (4.8), the spectral weighting function and the offset parameter (4.9), the number of arrivals to include, and the name of the completed simulation. Since the odd and even arrivals differ only in an attenuation constant and time delay, only the first two arrivals needed to be calculated to compute a complete simulation, with an arbitrary number of arrivals.

The code first read in the observed waveform and calculated the spectral weighting function. The full simulation was assembled by looping through all arrivals, applying the attenuation constant and spectral weighting function, applying any additional extra time delay (depending on the arrival), then summing the result into the final solution matrix. Finally the offset was calculated using the observed waveform (4.9). The offset was applied to the complete simulation and the results saved. At this point, from a numerical standpoint, the FDTD and empirical source model results were identical.

### **Reference**

M.D. Collins, R. J. Cederberg, D.B. King, and S.A. Chin-Bing, "Comparison of algorithms for solving parabolic wave equations" J. Acoust. Soc. Am. Volume 100, Issue 1, pp. 178-182 (1996).

## **APPENDIX B - RAM-PE CONVERGENCE**



The accuracy of solutions produced using the PE method is dependent on the convergence of the solution. That is, the  $q$  term rational approximation in equation (3.10) converges to the correct solution of the forward differential equation (3.8), for the given frequency and environmental configuration (i.e. bathymetry and sediment layers). Convergence is dependent upon the choice of certain input parameters. The parameters of most importance are the range and depth grid spacing,  $dr$  and  $dz$ , but the number of stability constraints and number of Padé terms (the number of terms in the  $q$  term rational approximation (3.8)) can also affect convergence. Typically, general rules are followed to obtain a correct grid spacing, such as  $dz = \lambda/10$ , but due to the requirement of broadband analysis, it was advantageous to obtain a uniform grid for all frequencies, and therefore avoid errors due to interpolation.

In general, finer spatial resolutions lead to convergence, however, especially for the low frequency, longer wavelength simulations; erroneous results can result from an over-fine spatial grid. Furthermore, a given grid can cause single frequency solutions to lose convergence entirely and produce extremely erroneous solutions. The cause of these glitches was the failure of the operator in (3.9) to satisfy the equation in forward differential equation (3.8), which was usually alleviated by changing the number of Padé terms calculated. Due to this, convergent parameters needed to be determined not only at the minimum and maximum frequencies, but also at several frequencies in the bandwidth. Furthermore, it was necessary to check each frequency solution for convergence. With these considerations, a uniform grid was defined for all frequencies, but also a frequency dependent number of Padé terms was also used (i.e. 500-1500 Hz, 5 Padé terms). Two stability constraints were used in all modeling.

The method for obtaining convergent parameters is called the convergence test. In this method, identical simulations are calculated, varying only the range and depth resolutions. The solutions that match those calculated with different spatial grids are convergent. Range and depth steps are varied by powers of 2 across a specified range, and for each range step, a solution is calculated for each depth step.

The convergence test method is illustrated in Figure B.1. Comparing Panels (A) and (B), there is very little difference between the output results, despite the different spatial grid sized. In the bottom of Panel (B), the TL curve from Panel (A) has been overlaid with the curve taken from Panel (B), and no difference can be seen. In Panel (C) however, the new curve is dramatically different, and this spatial grid is not considered to be convergent. This process is then repeated using different numbers of Padé terms and stability constraints in order to obtain a uniform convergent grid over all frequencies.

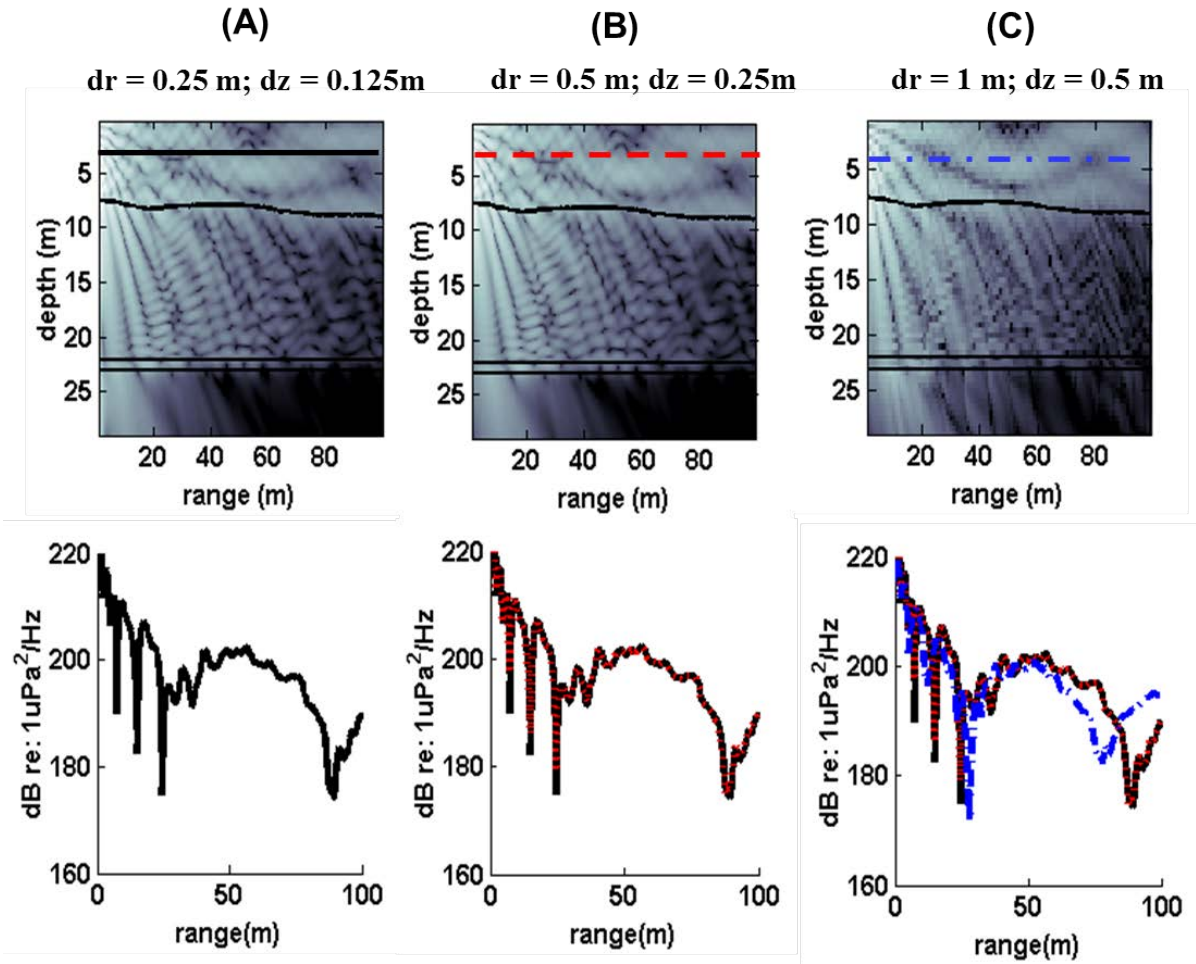


Figure B.1: Illustration of the convergence testing method. Panel (A), (B), and (C) show the results of otherwise identical simulations computed using different spatial grids, where the grid sized increase from left to right. The curves at the bottom of each panel are the TL lifted from the upper part of the frame at a depth of 4.5m.